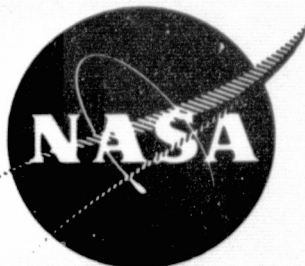


## **General Disclaimer**

### **One or more of the Following Statements may affect this Document**

- This document has been reproduced from the best copy furnished by the organizational source. It is being released in the interest of making available as much information as possible.
- This document may contain data, which exceeds the sheet parameters. It was furnished in this condition by the organizational source and is the best copy available.
- This document may contain tone-on-tone or color graphs, charts and/or pictures, which have been reproduced in black and white.
- This document is paginated as submitted by the original source.
- Portions of this document are not fully legible due to the historical nature of some of the material. However, it is the best reproduction available from the original submission.



INDUSTRIAL ION  
SOURCE TECHNOLOGY

PREPARED FOR  
LEWIS RESEARCH CENTER  
NATIONAL AERONAUTICS AND SPACE ADMINISTRATION  
GRANT 3086



Annual Report  
December 1978

Harold R. Kaufman  
and  
Raymond S. Robinson  
Department of Physics  
Colorado State University  
Fort Collins, Colorado

## TABLE OF CONTENTS

I. INTRODUCTION . . . . .	1
II. ION BEAM TEXTURING OF SURFACES . . . . .	3
III. SEEDING RATE FROM A BEVELED SOURCE . . . . .	29
IV. ENERGETIC BINARY COLLISIONS IN RARE GAS PLASMAS . . . . .	45
V. PHYSICAL SPUTTERING AND REACTIVE ION ETCHING . . . . .	55
VI. CONCLUDING REMARKS . . . . .	66
REFERENCES . . . . .	68

## I. INTRODUCTION

The overall objective of this grant is to further the industrial applications potential of ion-beam etching and deposition processes. To accomplish this overall objective, a variety of specific tasks have been undertaken. This report is divided into sections corresponding to the various tasks.

Extensive experimental studies of the ion beam texturing of surfaces were begun during the last support period<sup>1</sup> and have been continued and expanded. Primary emphasis has moved toward experimental checks on a surface texturing model developed during this past year.

An end objective of this task has been to develop convenient and reliable procedures for texturing a variety of surfaces. The textured surfaces could be used for functions such as the control of secondary electron emission, the increased absorption of light, and the improved attachment of biological tissue (for medical implants).

Textured surfaces, typically with conical structures, have been produced by simultaneously etching a surface and seeding that surface with another material. A model based on surface diffusion predicts a variation in cone spacing with surface temperature, as well as a critical temperature below which cones will not form. Substantial agreement with the model has been found for several combinations of seed and surface materials, including one with a high sputter yield seed on a low sputter yield surface (gold on aluminum). Coning with this last combination was predicted by the theory for a sufficiently mobile seed material. The existence of a minimum temperature for the formation of cones should also be important to those interested in ion-beam machining of smooth surfaces. Elements contained in environmental



contaminants or within the sputtered alloys or compounds may also serve as seed material.

A mathematical model has been developed to calculate the sputter deposition of seed material onto a substrate during texturing. The deposition rates calculated using this technique are used as inputs to the predictive model for cone formation and distribution.

Calculations have been continued on cross sections for energy and momentum transfer in binary collisions between like pairs of Ar, Kr, and Xe atoms in the energy range from about 1eV to 1000eV. These calculations were begun during the last support period using a classical model with pair interaction potentials for the rare gases developed from experimental sources, e.g., investigations of specific heats, viscosities, solid state parameters and scattering data.<sup>2</sup> Cross sections in this energy range have not been available. The cross sections exhibit a rapid decrease from accepted values at thermal energies as the interaction energy increases. This behavior can be used to understand directed beam propagation limits as well as particle propagation within a plasma.

Silicon has been successfully textured on a micron scale with a higher activation energy being indicated than is typical of metallic systems. Operation of an ion source and sputter etch rates have both been studied using reactive gases instead of Ar, the usual working gas.

## II. ION BEAM TEXTURING OF SURFACES

Ion beam sputtering is frequently used in surface etch or milling operations where the desired result is the uniform removal of material, perhaps using a mask to produce a relief pattern on a substrate, or simply as a thinning process such as sample preparation for transmission electron microscopy. The processed surfaces, however, are often not microscopically smooth but exhibit a variety of surface textures that develop as a result of the ion bombardment.

Textures can develop on solid surfaces in several ways during directed ion beam sputtering. Physical sputtering of solid materials, which is customarily accomplished using chemically inert ion species, can reveal individual crystal grains because of differential sputter etch rates dependent on crystal grain orientation. Impurities, precipitates, phases or initially irregular surfaces can also cause characteristic textures to develop during sputtering because of preferential etching of higher sputter yield sites.<sup>1</sup> In addition, reactive ion beam etching can chemically texture a surface through selective removal of elements from an alloy.<sup>2</sup>

Of particular interest here, however, is the texturing induced by the deliberate deposition of an impurity onto a solid surface while simultaneously bombarding the surface with an ion beam. This technique is often referred to as "seeding", with the impurity being termed the seed material. Under appropriate conditions, microscopic cones or hillocks develop because of preferential sputtering of surrounding material. It has been generally understood that these cones result from clusters of seed atoms protecting the underlying substrate while surrounding substrate material is etched away.<sup>3</sup>

Ion beam texturing has been attempted with many material combinations and has several potential applications. Textured surfaces have been successfully used for enhanced absorption of radiant energy in solar collectors.<sup>4</sup> Perhaps one of the more promising applications is in the realm of biomedical materials such as prostheses with soft or hard tissue interfaces that require firm bonding.<sup>5,6,7,8</sup>

It has been postulated that the formation and replenishment of seed clusters is a result of the surface diffusion or migration of seed atoms with nucleation or attachment occurring when other seed atoms are encountered. It has also been widely believed that a necessary, but possibly not a sufficient, condition for the formation of sputter cones is that the seed material must have a lower sputter yield than the substrate material to account for the observed differential etch. The validity of these ideas is explored within the context of an analytical model along with experimental tests.

A model has been developed as a first approximation to both a qualitative and quantitative description of the surface migration of seed atoms, the clustering process, and the resulting distribution of cones on a substrate. Experimentally controllable parameters as well as physical properties of the materials involved are included in the model. The diffusion aspect is described first. The critical minimum size of seed clusters is then related to the seed diffusion rate. As a further result, a critical substrate temperature is obtained, below which cones will not be formed by the diffusion and sputtering of seed material. The predictions based on this model are investigated experimentally and an assessment is made of the impact of the model on the variously held postulates and assumptions regarding the seeding and cone formation processes.

### Sputter Cone Seeding Theory

The primary features of a conceptual model used to understand seed diffusion are: 1) a substrate surface characterized as an array of uniformly distributed adsorption sites at which seed atoms can be bound to the surface after being deposited onto the substrate; 2) these individual adsorption sites described as potential energy minima that interact with seed atoms through isotropic binding and restoring forces; 3) the seed atoms of sizes and masses appropriate to the seeding species used that are deposited onto the substrate through some external means; and 4) an ion beam of a given energy and type of ion providing a uniform flux density of energetic ions over the substrate.

#### Surface Diffusion

The frequency for an isolated seed atom, located at an adsorption site and belonging to a population of adsorbed seed atoms in thermal equilibrium with a substrate of temperature  $T$ , to jump between adsorption sites is

$$\nu = (1/\tau_0) \exp (-E_d/kT) , \quad (2-1)$$

where  $\tau_0$  is the characteristic time for the jumping process,  $E_d$  is the activation energy for diffusion (i.e., the energy barrier between adsorption sites) and  $k$  is Boltzmann's constant. The exponential factor reflects the probability that, given thermal equilibrium at temperature  $T$ , a seed atom has an energy greater than  $E_d$ , assuming a uniform density of states. The reciprocal of the characteristic time  $\tau_0$  may be thought of as a characteristic frequency of oscillation for the seed atom in the potential well representing the adsorption site.

The total number of adsorption sites visited by an adsorbed seed atom during the time that it spends on the surface is given by the jump frequency  $\nu$  multiplied by the mean adsorption time  $\tau_a$ :

$$n_a = \nu \tau_a = (\tau_a/\tau_o) \exp (-E_d/kT) . \quad (2-2)$$

The magnitude of the mean adsorption time  $\tau_a$  is governed by those processes that would tend to remove or desorb a seed atom from the surface. One candidate process would be evaporation or sublimation which would occur if a seed atom possessed simultaneously sufficient energy to break the adsorption bond and a momentum directed away from the surface. If the seed atoms are considered to be in thermal equilibrium with the substrate, the probability of having sufficient energy to desorb would be  $\exp(-E_o/kT)$  where  $E_o$  is the total binding energy of the seed atom to the surface. Clearly,  $E_o > E_d$ , making this process highly improbable. A more likely mechanism for removal of adsorbed seed atoms is physical sputtering by an applied high current density ion beam. The probability of a seed atom being sputtered depends linearly on the ion flux and on the seed cross section.

The migration of seed atoms along the surface of the substrate can be viewed as a random-walk process. Using  $a_o$  as the mean distance between adsorption sites, the random-walk diffusion length  $r_d$  is given by

$$r_d = a_o n_a^{1/2} = a_o (\tau_a/\tau_o)^{1/2} \exp (-E_d/2kT) . \quad (2-3)$$

The random-walk diffusion length represents the average net separation distance of a seed atom from its initial adsorption site, achieved

during a time  $\tau_a$ . This, then, is the average radius through which seed atoms are expected to be able to diffuse. This expression (Eq. (2-3)) is similar to diffusion equations derived for condensation of a vapor phase onto a substrate. It is necessary to obtain appropriate values for  $\tau_a$  and  $\tau_o$  to apply this equation to the seeding and texturing problem.

The seed adsorption time is limited by the ion beam sputter removal of seed atoms once they are attached to the surface. If the ion flux (ions/m<sup>2</sup>-sec) is given by  $R_i$  and the cross section that a seed atom presents to the ion beam is given by  $\sigma_a$  then the probability per unit time  $P_c$  for individual ion-seed collisions to occur is

$$P_c = R_i \sigma_a . \quad (2-4)$$

The probability that a given collision will result in removal of an atom is the sputter yield or sputter probability  $Y_a$ . Thus, the probability per unit time  $P_s$  for sputter removal of individual seed atoms from the substrate is

$$P_s = Y_a R_i \sigma_a . \quad (2-5)$$

The reciprocal of this probability per unit time is then the mean adsorption lifetime for a seed atom on the substrate

$$\tau_a = \frac{1}{P_s} = 1/Y_a R_i \sigma_a \quad (2-6)$$

A first estimate of  $\tau_a$  can be obtained by inserting approximate values for the quantities in Eq. (2-6). For a loosely bonded and mobile seed

atom, the sputtering yield  $Y_a$  should be near unity. The cross section  $\sigma_a$  can be approximated as  $N_o^{-2/3}$ , where  $N_o$  is the atomic density of the substrate with a typical value of  $10^{29} \text{ m}^{-3}$ .<sup>9</sup> The value of  $R_i$  for a typical  $10 \text{ A/m}^2$  ( $1 \text{ mA/cm}^2$ ) ion beam current density is about  $6 \times 10^{19} (\text{m}^2\text{-sec})^{-1}$ . With these substitutions an adsorption time of about  $1/3$  sec is obtained.

Seed atoms of interest in the process of sputter cone formation must be mobile. The seed atoms should therefore exhibit weaker bonding to the substrate than that of the substrate atoms to one another. Because of this relatively weak bonding for seed atoms, the characteristic time  $\tau_o$  for a seed atom to jump between adsorption sites should be a function of this bonding interaction, rather than the substrate lattice vibrations to which it is only loosely coupled. Considering a seed atom at an adsorption site, the site can be thought of as a potential well within which the seed atom is bound. The potential barrier between adjacent sites is the activation energy  $E_d$ . Motion along the surface should therefore be characterized by a well depth  $E_d$  and an approximate periodicity. Using  $a_o$  as the average spacing between sites, a sinusoidal representation of a periodic, undulating potential is

$$U(r) \approx E_d(1 - \cos 2\pi r/a_o)/2 . \quad (2-7)$$

A parabolic potential results from retaining only the first two terms in the cosine series expansion.

$$U(r) \approx \pi^2 E_d r^2 / a_o^2 \quad (2-8)$$

Using  $m_s$  as the mass of the seed atom, the equation of motion is

$$m_s d^2 r / dt^2 = -\partial U(r) / \partial r = -2\pi^2 E_d r / a_o^2, \quad (2-9)$$

which implies an harmonic oscillation frequency of

$$\nu = (E_d / 2m_s a_o^2)^{1/2}, \quad (2-10)$$

or a period of

$$\tau_o = (2m_s a_o^2 / E_d)^{1/2} \quad (2-11)$$

This expression probably underestimates somewhat the time to jump between adsorption sites because of the parabolic approximation that was assumed. A numerical estimate of  $\tau_o$  can be obtained using the appropriate substitutions. The distance  $a_o$  can be approximated as  $N_o^{-1/3}$ , with  $N_o$  again the atomic density. The mass  $m_s$  of a representative heavy seed atom can be taken as  $3 \times 10^{-25}$  kg, while the activation energy  $E_d$  may be assumed to be in the neighborhood of  $1.6 \times 10^{-19}$  J (1eV).<sup>10</sup> With these substitutions,  $\tau_o$  is found to be about  $4 \times 10^{-13}$  sec.

Using Eqs. (2-6) and (2-11) to substitute for  $\tau_a$  and  $\tau_o$  in Eq. (2-3):

$$\tau_d = (E_d / 2m_s)^{1/2} (a_o / R_i Y_a \sigma_a)^{1/2} \exp(-E_d / 2kT) \quad (2-12)$$

With the substitutions of  $N_o^{-1/3}$  and  $N_o^{-2/3}$  for  $a_o$  and  $\sigma_a$ , together with unity for  $Y_a$ , a simplified expression is obtained,



$$r_d = (E_d/2m_s)^{1/4} (N_o^{1/3}/R_i)^{1/2} \exp(-E_d/2kT) \quad (2-13)$$

The exponential factor varies rapidly over a wide range. The square-root factor is much more slowly varying, so that numerical values may be substituted therein for a first approximation. Making the substitutions of  $1.6 \times 10^{-19}$  J for  $E_d$ ,  $10^{29} \text{ m}^{-3}$  for  $N_o$ ,  $3 \times 10^{-25}$  kg for  $m_s$  and  $6 \times 10^{19} (\text{m}^2\text{-sec})^{-1}$  for  $R_i$  in the square-root factor,

$$r_d = 2 \times 10^{-4} \exp(-E_d/2kT) \quad (\text{m}) \quad (2-14)$$

This, then, is an estimate of the radius over which surface diffusion can be expected to take place. This radius is a function primarily of the activation energy  $E_d$  and the substrate temperature. Other factors such as seed atom mass  $m_s$ , ion flux  $R_i$ , and the adsorption site spacing  $a_o$  are considerably less important. The activation energy is a function of the seed-substrate material combination (together with a small temperature effect) and ranges from about 0.5 to 2eV for metallic materials of interest for seeding.<sup>11</sup> The large variation of  $r_d$  with temperature is shown in Fig. 2-1 for this range of activation energies. It can be seen that relatively modest temperature changes can have a profound effect on the mean seed diffusion radius.

A distance equal to twice the average diffusion radius can be used as a measure of the average separation between clusters. If clusters were, on the average, much farther apart than  $2r_d$ , more clusters would begin to nucleate and grow in the intervening spaces where seed densities were enhanced, thus narrowing the gaps between clusters.

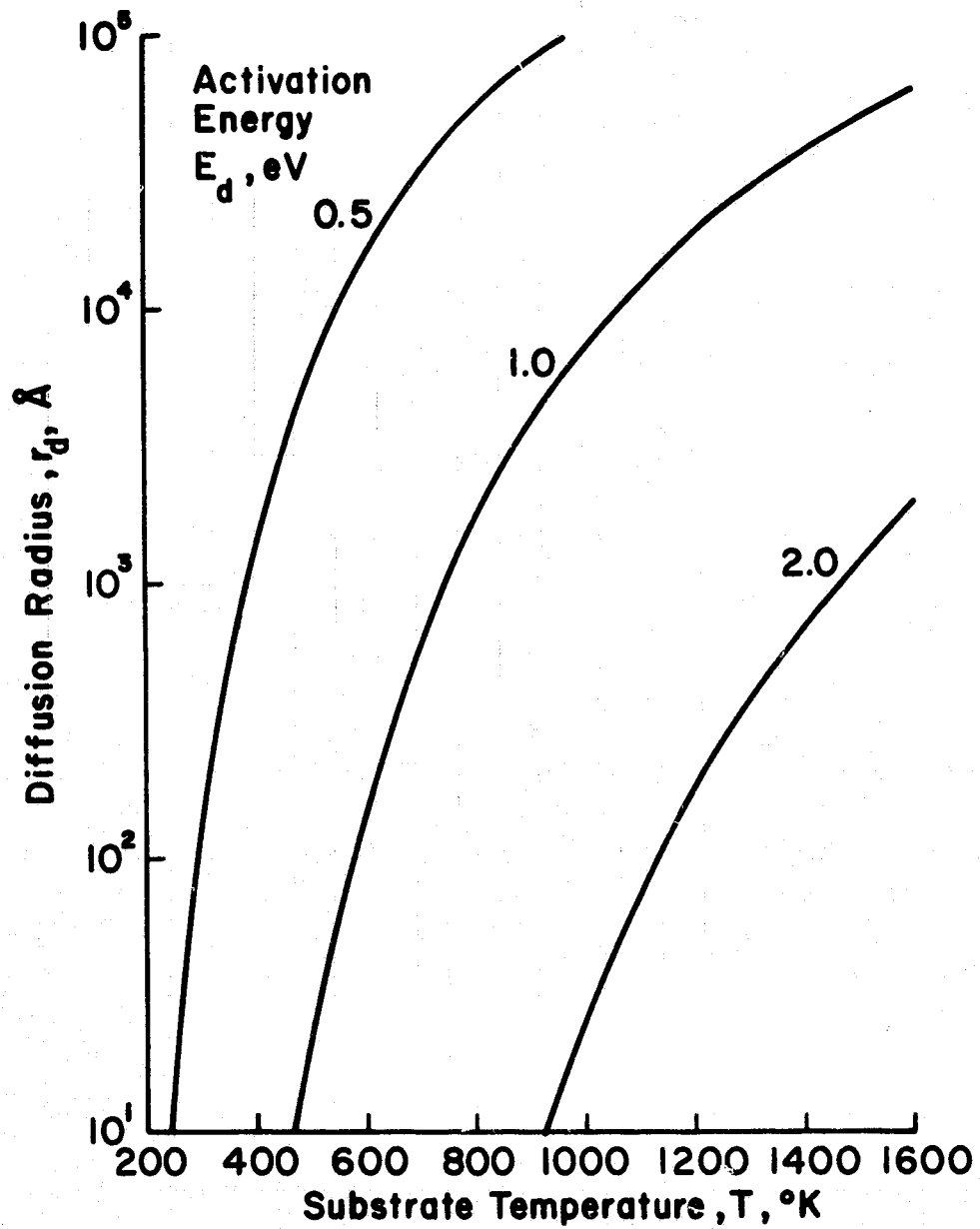


Fig. 2-1. Diffusion radius as a function of activation energy and substrate temperature for a specific case.

At the other extreme, if clusters began to nucleate at separations much less than  $2r_d$ , larger clusters would grow faster and intercept diffusing seed material at the expense of smaller clusters. Thus, an average cluster separation of about  $2r_d$  would be expected to be stable.

### Seed Clustering

Having found the radius from which diffusion will supply a seed cluster, it is appropriate to consider the stability of that cluster. There is a critical size of a seed cluster, below which steady growth is not possible.<sup>12</sup> This critical radius is essentially the same value as is used in nucleation theory. It is obtained by setting to zero the derivative of free energy (surface plus volume) with respect to radius.<sup>13</sup> Continuous growth can take place above this radius, but dissociation of the cluster will tend to occur at smaller radii.

Whether or not a seed cluster is stable will therefore depend on the diffusion rate to the cluster being sufficient, or insufficient, to supply the sputtering loss from a cluster of critical radius. To determine the stability requirements of seed clusters it is necessary to investigate more closely the processes of seed movement, and clustering while adsorbed on a substrate.

Seed atoms are assumed to move from adsorption site to adsorption site on the surface by a random walk process. Only those seed atoms that acquire an energy greater than  $E_d$  are mobile. Energy is exchanged between seed atoms and the lattice through the loose coupling of the seed atom to thermal lattice vibrations bringing the adsorbed seed atom population into approximate thermal equilibrium with the

substrate lattice. It is then the temperature of the substrate that governs the fraction of seed atoms that are mobile at any given time. A random walk process for seed motion requires that, on the average, seed atoms experience an inelastic "collision" as a result of each jump to a neighboring adsorption site. The energy loss in the inelastic process would then be associated with a loss of the initial direction of motion resulting in a random direction for the next jump. Regarding each jump to a neighboring adsorption site as an independent event terminating with directional and energy losses can be further supported by considering the adsorption bonding forces tending to accelerate a seed atom down into the neighboring adsorption site once it has cleared the potential barrier  $E_d$ , where  $E_d$  is the diffusion activation energy. It is improbable that the incoming seed velocity vector would be sufficiently well-aligned with the spatial symmetry of the neighboring adsorption site to proceed without significant deflection.

To appropriately model the clustering of seed atoms, it is first necessary to characterize the mean speed for the surface migration of seed atoms. There is the possibility of assigning different characteristic velocities to mobile seed atoms. One velocity, designating the micro-velocity  $v_m$ , could be derived from the spacing of adsorption sites and the jump time,

$$v_m = \frac{a_o}{\tau_o} \quad (2-15)$$

or, using Eq. (2-11),

$$v_m = (E_d/2m_s)^{1/2} \quad (2-16)$$

Substituting 1eV for  $E_d$  and  $3 \times 10^{-25}$  Kg for  $m_s$  yields,

$$v_m = 5.2 \times 10^2 \text{ m/sec} . \quad (2-17)$$

Another velocity, designated macro-velocity  $v_M$ , can be obtained from the random walk diffusion radius and the mean adsorption time,

$$v_M = r_d / \tau_a \quad (2-18)$$

or, using Eqs. (2-6) and (2-13),

$$v_M = (E_d / 2m_s)^{1/4} (R_i Y_a^2 / N_o)^{1/2} \exp(-E_d / 2kT) . \quad (2-19)$$

Using the representative values of 1eV for  $E_d$ ,  $6 \times 10^{19} \text{ m}^{-2} \text{ sec}^{-1}$  for  $R_i$ , 1 for  $Y_a$ ,  $3 \times 10^{-25}$  Kg for  $m_s$ ,  $10^{29} \text{ m}^{-3}$  for  $N_o$ , and 800°K for T we get

$$v_M = 4.0 \times 10^{-7} \text{ m/sec} . \quad (2-20)$$

This is nine orders of magnitude less than  $v_m$ . Perhaps a more appropriate expression for the seed velocity would take into account the total distance of travel found by summing all jumps taken in a seed lifetime  $\tau_a$ . The number of jumps is given by Eq. (2-2):

$$n = (\tau_a / \tau_o) \exp(-E_d / kT) , \quad (2-21)$$

and the mean seed speed is:

$$v_s = na_o/\tau_a , \quad (2-22)$$

or, using Eqs. (2-21) and (2-11)

$$v_s = (E_d/2m_s)^{1/2} \exp (-E_d/kT) , \quad (2-23)$$

or,

$$v_s = 2.6 \times 10^{-4} \text{ m/sec} \quad (2-24)$$

with the usual substitutions. Equation (2-23) then, is felt to be the most appropriate expression for average seed velocity for the purpose of understanding diffusion and clustering.

With an expression for seed velocity, the detailed movements of seed atom populations will now be considered. As a first example, an estimate for the upper bound of the areal density of seed atoms on the substrate,  $N_s$ , can be obtained by assuming that clusters fail to form on a seeded surface. In the absence of seed clusters, a steady state will be reached with the seed deposition rate and the re-sputtering rate being equal. The seed flux  $R_s$  (seed atoms deposited/m<sup>2</sup>-sec) can be written in terms of the ion flux using a factor  $F_s$ , the seeding fraction, that reflects the ratio of seed deposition to ion flux:

$$R_s = F_s R_i . \quad (2-25)$$

The rate of seed removal by physical sputtering  $S_s$  is the probability per unit time for sputtering an individual seed atom multiplied by the

areal seed density  $N_s$

$$S_s = Y_a R_i \sigma_a N_s . \quad (2-26)$$

Equating the deposition and sputter removal rates gives,

$$F_s R_i = Y_a R_i \sigma_a N_{s_{\max}} , \quad (2-27)$$

where  $N_{s_{\max}}$  is the maximum achievable areal seed density in the absence of clustering. Solving for  $N_{s_{\max}}$ :

$$N_{s_{\max}} = F_s / Y_a \sigma_a . \quad (2-28)$$

With a value of 0.01 for  $F_s$ , this expression yields, using the customary substitutions:

$$N_{s_{\max}} \approx 2 \times 10^{17} \text{ m}^{-2} . \quad (2-29)$$

We can also look at the fraction of surface coverage by seed atoms.

Since  $1/\sigma_a$  is approximately the density of adsorption sites we get

$$F_s N_a \approx N_s \quad (2-30)$$

where  $Y_a$  has been assumed to be approximately 1 and  $N_a$  is the adsorption site density. Thus, the maximum fractional surface coverage by seed material is about equal to the seeding fraction  $F_s$ .

A more detailed analysis is necessary when clusters are assumed to be present on the substrate. Figure 2-2 represents a cluster and its surrounding seed diffusion area. The various  $\dot{N}$ 's shown in Fig. 2-2 are flow rates of seed atoms in atoms/sec. Let  $N_c$  be the areal density

of seed clusters, then  $1/N_c = A = A_c + A_d$ , where  $A_c$  is the cluster area and  $A_d$  is the diffusion 'drawing' area. The definitions of the seed flow rates are in Table 2-1.

Table 2-1. Seed Flow Rates

$\dot{N}_1$	Seed atom deposition rate into area $A_d$
$\dot{N}_2$	Seed atom deposition rate into area $A_c$
$\dot{N}_3$	Rate of seed atom acquisition by the cluster
$\dot{N}_4$	Rate of re-sputtering of seed atoms from $A_d$
$\dot{N}_5$	Rate of re-sputtering of seed atoms from $A_c$
$\dot{N}_6$	Rate of diffusion of seed atoms out of $A_d$
$\dot{N}_7$	Rate of diffusion of seed atoms into $A_d$

All rates,  $\dot{N}_i$  are positive with the direction of seed flow indicated by the arrows in Fig. 2-2.

A steady state situation will be considered first. Under steady state conditions, the following relations hold:

$$\dot{N}_6 = \dot{N}_7 \quad (2-31)$$

$$\dot{N}_1 + \dot{N}_2 = \dot{N}_4 + \dot{N}_5 \quad (2-32)$$

$$\dot{N}_1 - \dot{N}_4 = \dot{N}_3 \quad (2-33)$$

$$\dot{N}_2 + \dot{N}_3 = \dot{N}_5 \quad (2-34)$$



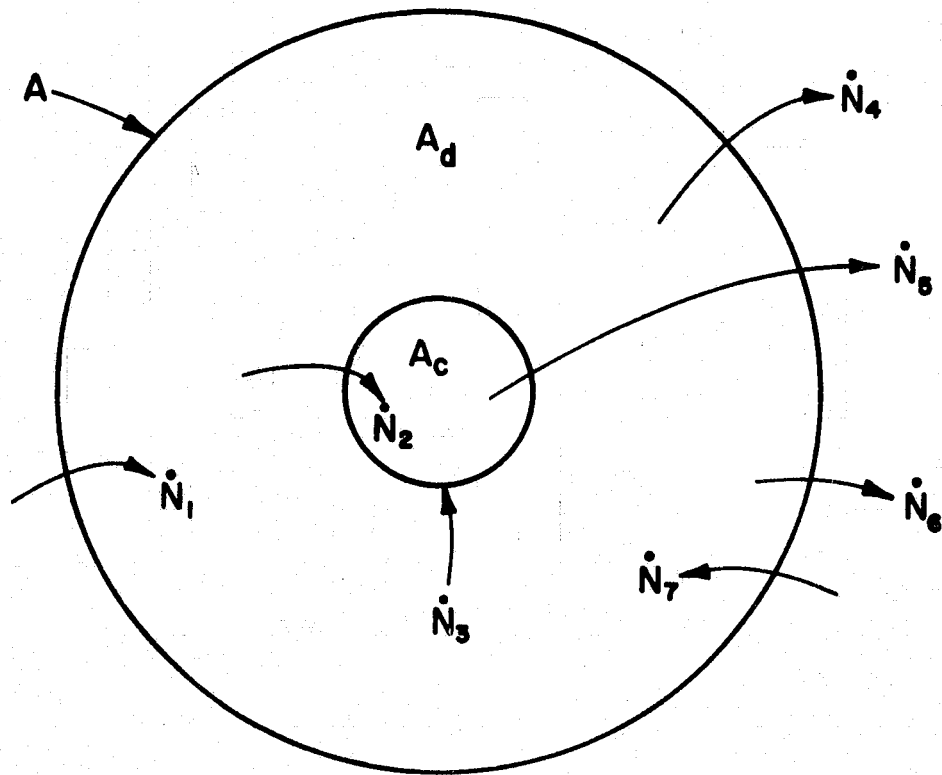


Fig. 2-2. Geometrical representation of a cluster of seed atoms of area  $A_c$  with the surrounding area  $A_d$ . Seed atom fluxes are represented by arrows.

Equation (2-31) simply expresses the symmetry of seed diffusion into and out of the area A containing a single cluster. Equation (2-32) equates the total seed deposition rate to the total sputter removal rate in area A. Equation (2-33) relates the net seed flux into  $A_d$  (taking re-sputtering into account) to the diffusion flux from  $A_d$  to the cluster. Finally, Eq. (2-34) equates the total flux to the cluster to the total sputtering from the cluster. Equation (2-32) can be obtained by eliminating  $\dot{N}_3$  between Eqs. (2-33) and (2-34).

Most of the individual rates can be obtained from consideration of simple sputtering rates:

$$\dot{N}_1 = R_i F_s A_d \quad (2-35)$$

$$\dot{N}_2 = R_i F_s A_c \quad (2-36)$$

$$\dot{N}_4 = R_i Y_a \sigma_a N_s A_d \quad (2-37)$$

$$\dot{N}_5 = R_i Y_c A_c \quad (2-38)$$

where  $Y_c$  is the sputter yield of atoms from the seed cluster.  $\dot{N}_3$  is related to the 'collision' frequency of seeds with clusters. Assuming that each seed colliding with a cluster adheres we can use a length of  $2r_c$  to describe the two-dimensional cluster interaction cross section where  $r_c$  is the cluster radius.

$$\dot{N}_3 = 2r_c v_s N_c N_s A_d \quad (2-39)$$

This relation can be understood more simply by noting that  $2r_c v_s N_c$  is the collision frequency for a single seed moving through clusters of density  $N_c$  at a speed  $v_s$ . Multiplying by the number of seed atoms per unit area gives the total frequency of seed-cluster collisions per unit area. Multiplying by the "drawing" area  $A_d$  for a single cluster gives the number of collisions with one cluster per unit time.

With substitutions for the various rates, Eqns. (2-33) and (2-34) can be rewritten as:

$$R_i F_s A_d - R_i Y_a \sigma N_s A_d = 2r_c v_s N_c N_s A_d \quad (2-40)$$

and

$$R_i F_s A_c + 2r_c v_s N_c N_s A_d = R_i Y_c A_c \quad (2-41)$$

These equations may be solved simultaneously for the drawing area  $A_d$  and for the surface seed density  $N_s$ .

$$A_d = \frac{A_c (Y_c - F_s) (2r_c v_s + A_c Y_a \sigma R_i)}{2r_c v_s F_s - A_c (Y_c - F_s) Y_a \sigma R_i} \quad (2-42)$$

$$N_s = \frac{A_c (Y_c - F_s) R_i}{2r_c v_s} \left( 1 + A_c / A_d \right) \quad (2-43)$$

Under typical seeding and sputtering conditions the additive terms in Eq. (2-42) involving the ion arrival rate can be neglected giving:

$$A_d \approx A_c (Y_c - F_s) / F_s \quad (2-44)$$

Physically, this approximation corresponds to the actual seed coverage between clusters being much smaller than the maximum possible coverage. Equation (2-44) can be written in terms of  $r_d$  assuming circular geometry.

$$r_d = r_c [(Y_c - F_s)/F_s]^{1/2} \quad (2-45)$$

This is the required diffusion radius to sustain a seed cluster of critical radius  $r_c$ . For most applications,  $F_s \ll Y_c$ , so that  $F_s$  may often be neglected in the numerator with little error.

#### Critical Temperature

This diffusion radius (Eq. (2-45)) can be equated to that of Eq. (2-12) to determine the minimum substrate temperature that will give the required diffusion to sustain clusters of the minimum size.

$$T_c = E_d / k \ln \left[ (E_d / 2m_s)^{1/2} \left( F_s N_o^{1/3} / R_i Y_a r_c^2 (Y_c - F_s) \right) \right] \quad (2-46)$$

The logarithmic factor will vary slowly with changes in the variables therein; thus, the activation energy will most strongly dominate the critical temperature. The new variables that have been introduced are the critical radius  $r_c$  and the seeding fraction  $F_s$ . The seeding fraction is calculated in Section III, a value of 0.01 will be used as a reasonable approximation. Values of the critical radius range from about 6 to 10 Å.<sup>14</sup> A cross check was made on these values of  $r_c$  from another point of view. The use of a critical radius derived from nucleation studies implies perturbations corresponding to thermal energy. The energy of an ion impact in a sputtering environment, however, is far above the thermal level. The limiting condition for

ion impact is that the cluster should be large enough to absorb all the ion energy without vaporizing. The heat of sublimation for typical seed materials ranges from about 3 to 9eV/atom.<sup>15</sup> For typical ion energies of 500 to 1000eV, then, this minimum cluster radius is about 5 Å to 10 Å. The heat of sublimation is, of course, a macroscopic quantity. However, this calculation indicates that the increase in cluster size to accomodate the maximum perturbation of an ion collision should be moderate, almost certainly less than a factor of two times the nucleation theory radius of 10 Å.

Using 10 Å for  $r_c$  and 0.01 for  $F_s$  an approximate expression can be obtained for  $T_c$  in terms of the activation energy measured in eV for this expression only.

$$T_c \approx 587^\circ K E_d \quad (2-47)$$

This expression may be used for rapid estimates and approximations without paying undue attention to the precise values used for some of the other quantities.

#### Experimental Results and Discussion

Two physical effects following from the cone seeding theory were investigated experimentally: (1) the variation in cone density with substrate temperature, and (2) the existence of a critical temperature for cone formation. In the experiments, samples of aluminum were heated to a specified temperature and sputtered for 20 min. using a 1 mA/cm<sup>2</sup> beam of 500eV Ar ions, while simultaneously seeding the sample with a source of either Mo or Au. The specified substrate temperatures

ranged from 400 to 575°C in different tests, with In used to assure good thermal contact between the samples and the heat source.

Seeding was accomplished by partially covering the sample with a sheet of the seed material. Seed material was then sputtered from the beveled edge of this covering sheet onto the sample. Because of this geometrical arrangement, the seeding intensity decreased with increasing distance from the beveled edge (see Section III). After sputtering, scanning electron micrographs were obtained of the sample surfaces. The average separation between cones was then  $(A/N)^{1/2}$ , where  $N$  is the number of cones counted in an area  $A$  of the micrograph.

We identify  $\langle r \rangle$ , one half the average separation between cones, with the diffusion radius  $r_d$  in the preceding theory. Figures 2-3 and 2-4 show plots of  $\langle r \rangle$  as a function of reciprocal temperature for the two seed materials. From the theory, we expect straight lines on these plots. This can be shown by rewriting Eq. (2-13) as

$$r_d = r_o \exp(-E_d/2kT) \quad (2-48)$$

where  $r_o$  is a constant

$$r_o = (E_d/2m_s)^{1/4} (N_o^{1/3}/R_i Y_a)^{1/2} . \quad (2-49)$$

Taking the natural logarithm of Eq. (2-49) and rearranging the result,

$$\ln r_d = (-E_d/2k) 1/T + \ln r_o . \quad (2-50)$$

This expression is linear if  $\ln r_d$  is plotted as a function of inverse

temperature, as done in Figs. 2-3 and 2-4. The slope of the line is  $-E_d/2k$ , while the ordinate intercept is  $r_o$ .

A least squares regression line was fitted to each of Figs. 2-3 and 2-4. The best fit corresponded to an  $E_d$  of 1.20eV and an  $r_o$  of  $1.10 \times 10^7 \text{ \AA}$  for Fig. 2-3 and an  $E_d$  of 1.04eV and an  $r_o$  of  $6.04 \times 10^6 \text{ \AA}$  for Fig. 2-4. The correlation coefficients exceeded 0.9 for both fits. Experimental critical temperatures were also determined: 700°K for Al seeded with Mo and 675°K for Al seeded with Au.

The qualitative trends shown in Figs. 2-3 and 2-4 are all consistent with theory. The data shown also include varying distances from the edge of covering sheet, which corresponded to different seed ratios  $F_s$ . The only data selection used was that regions far enough from the covering sheet (low enough seed ratio) showed large fractions of the areas without cones and were omitted. For regions with sufficient seed to show fully developed cone structures, then, the effect of seed fraction  $F_s$  on cone spacing must be small. This result is in agreement with Eq. (2-13), which does not include  $F_s$  as a variable. Activation energies for surface diffusion were not available from literature for the exact combinations of materials used, but the values obtained from the slopes of Figs. 2-3 and 2-4 are in qualitative agreement with other combinations that have been studied using standard diffusion measurement techniques.

The activation energies from Figs. 2-3 and 2-4 can be used for a more quantitative comparison of experimental results with theory. Using these activation energies together with  $6.24 \times 10^{19} \text{ ions/m}^2\text{-sec}$  for  $R_i$ , .01 for  $F_s$ ,  $1 \times 10^{-9} \text{ m}$  for  $r_c$ , and handbook values for other variables, theoretical values were calculated for  $r_o$  and the

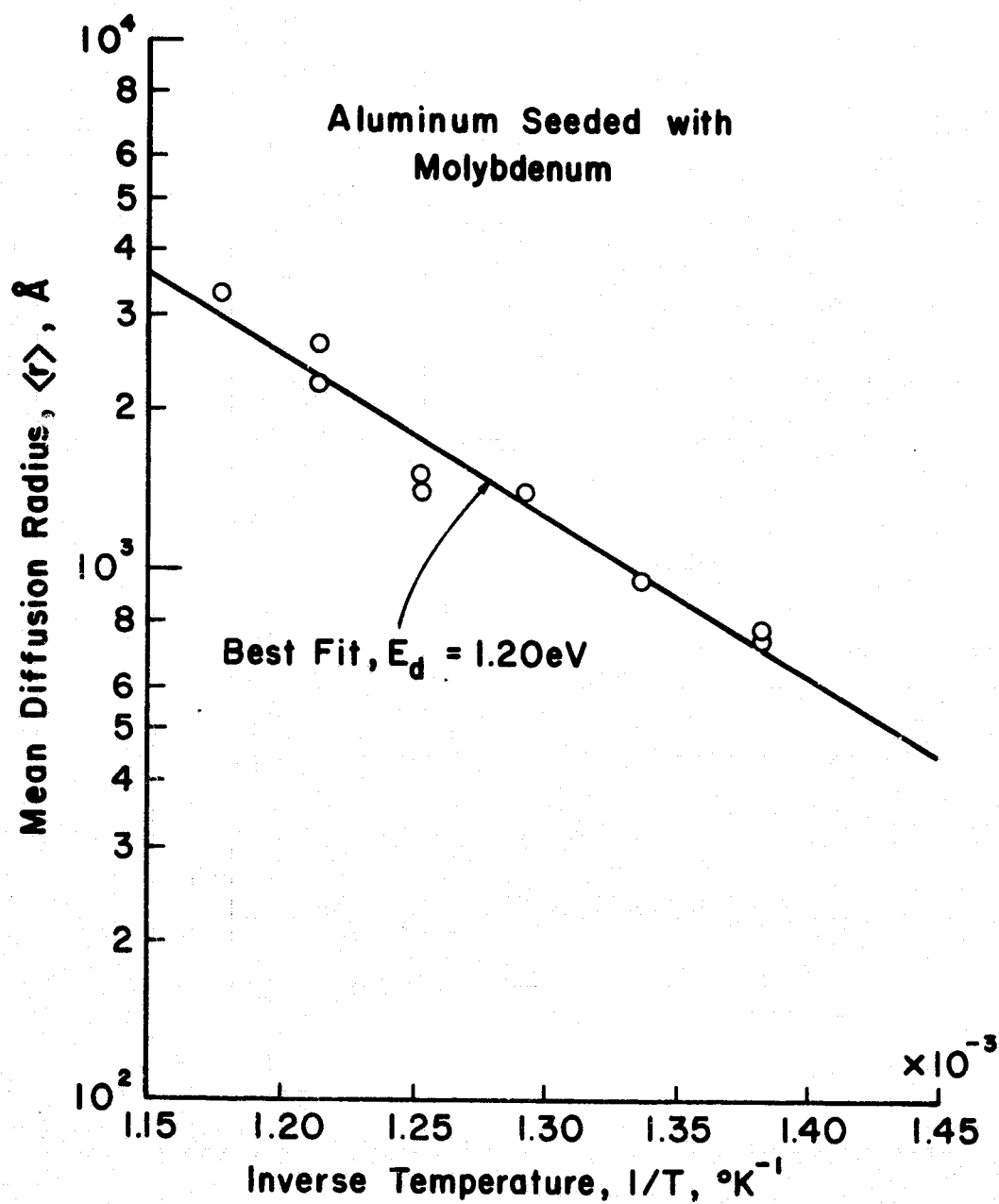


Fig. 2-3. Correlation for Al seeded with Mo.



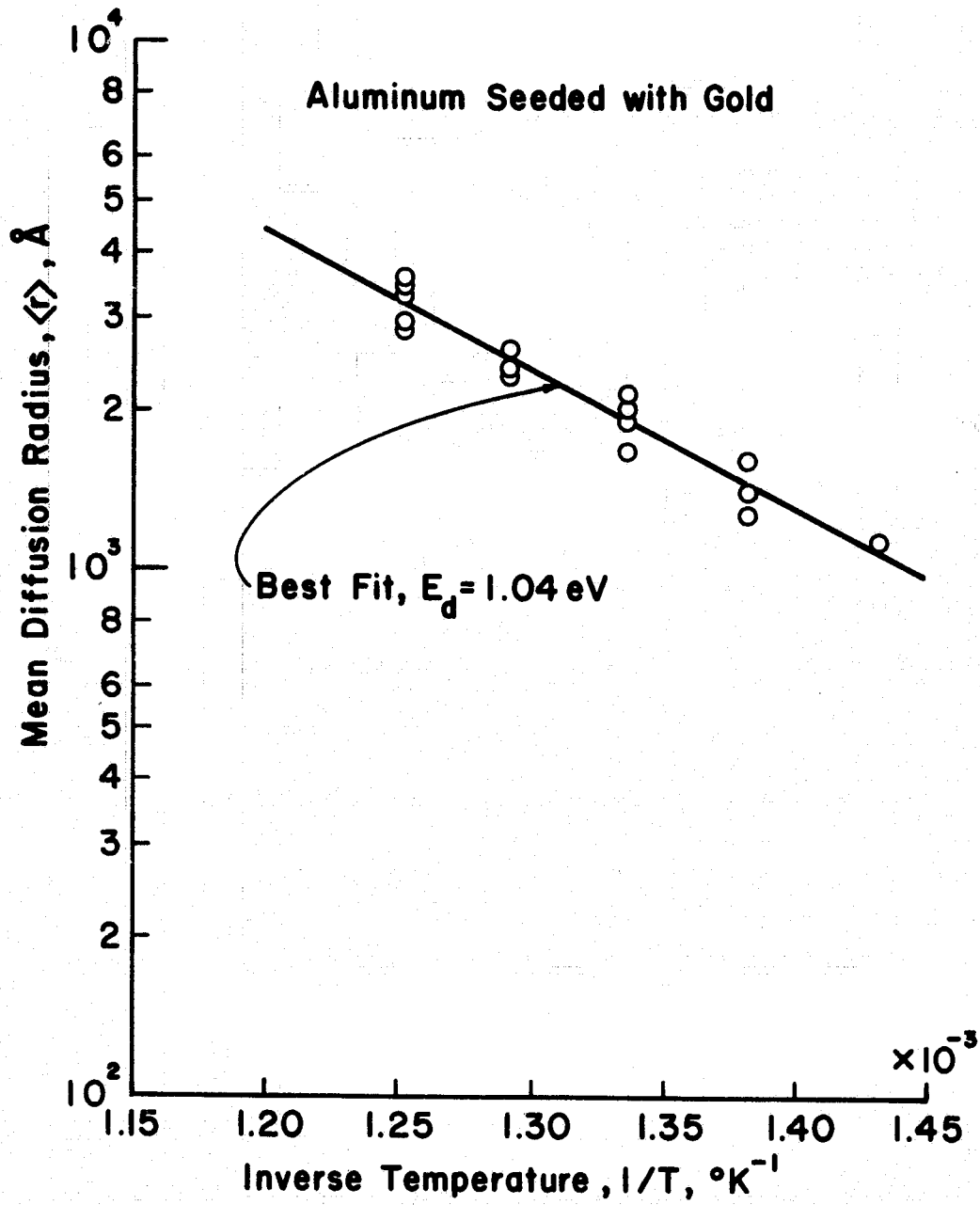


Fig. 2-4. Correlation for Al seeded with Au.

critical temperature. These values were  $2.21 \times 10^6 \text{ \AA}$  and  $684^\circ\text{K}$  for Al seeded with Mo and  $1.78 \times 10^6 \text{ \AA}$  and  $646^\circ\text{K}$  for Al seeded with Au. The agreement for critical temperature is close, with experimental values being 2 and 4 percent above the theoretical values from Eq. (2-46). This close agreement is due in part to most of the variables in Eq. (2-46) being included in a logarithmic factor. Closer agreement is to be expected between the predictions of the model and experimental results for the critical temperature than for other aspects of the model. For example, a limiting case of a flat surface as used in this model is more appropriate for derivation of the critical temperature at which no cones are present than for determining cone separation on a fully developed surface. The agreement for cone spacing is less close, with experimental values of  $r_0$  and cone spacing being 3 to 5 times the theoretical ones from Eq. (2-13). This difference may be the result of theory being derived for a flat isotropic surface, while the experimental values were for well developed conical surfaces. The cascades of sputtered substrate atoms on the conical surfaces would be expected to reduce seed diffusion toward the apexes, resulting in the reduction of some seed clusters below the critical size.

The choice of materials for Fig. 2-4 also represents support for the theory. Previous descriptions of coning states that low sputter yield materials protected the apexes of cones in higher sputter yield substrates. The present theory indicates that the seed can have a higher sputter yield than the substrate if the seed material is sufficiently mobile to replenish the sputtering loss from a seed cluster. The Au seed in Fig. 2-4 has a much higher yield than the Al substrate, so that this result is an example of coning that was predicted by the present theory.

A texturing theory based on surface diffusion has shown substantial agreement with experimental results. The existence of a minimum substrate temperature for texturing, the variation of cone spacing with temperatures and the texturing with a high sputter yield seed on a lower sputter yield substrate were all predicted by this theory. This theory has obvious utility in the production of textured surfaces for applications such as low reflectance solar cells, high emissivity heat radiators, and medical implants. The existence of a minimum critical temperature for coning is also important for the production of smooth surfaces, in that a sufficient reduction in surface temperature should reduce the mobility of any seed material enough to avoid coning, whether the seeding is due to stray sputtering or one of the elements in the substrate material. Due to the continual cleaning of the surface by the bombarding specie, the coning process also permits evaluation of the surface diffusion activation energy under conditions of extreme cleanliness.

### III. SEEDING RATE FROM A BEVELED SOURCE

Experimental arrangements for ion beam texturing include a beveled source of seed material placed on top of a substrate. Part of the substrate is covered with the seed source providing a control surface for comparison with the part that is uncovered and exposed to both sputter deposition of seed material and ion bombardment. Such an arrangement is shown in Fig. 3-1. This study will focus on the deposition rate of seed material onto the substrate from such a beveled surface.

A number of assumptions will be implicit in this seeding rate model. The ion beam will be assumed to have uniform current density over the area of interest and the beam will be directed normal to the substrate surface. The emission of sputtered seed atoms from points on the beveled edge will be assumed to correspond to a cosine distribution about the local surface normal. This assumption is in close agreement with experimental observations where only small departures from a cosine distribution have been observed.<sup>1,2,3,4,5</sup>

To model in detail the emission of sputtered atoms from the beveled surface and their subsequent deposition onto the substrate, we explore the geometry indicated in Fig. 3-2. Let  $d\Gamma_2$  be the rate of sputtered particle collection at the element of area  $da_2$  in particles per unit time arriving from the element of area  $da_1$ . This rate is proportional to the fraction of hemispherical solid angle subtended by  $da_2$  as viewed from  $da_1$ , i.e.,  $da_2 \cos \phi_2 / 2\pi r^2$ . The emission from  $da_1$  in the direction  $\phi_1$  is proportional to  $da_1 \cos \phi_1$  because of the assumed cosine emission distribution. The emission from  $da_1$  arriving at  $da_2$  can thus be expressed as:

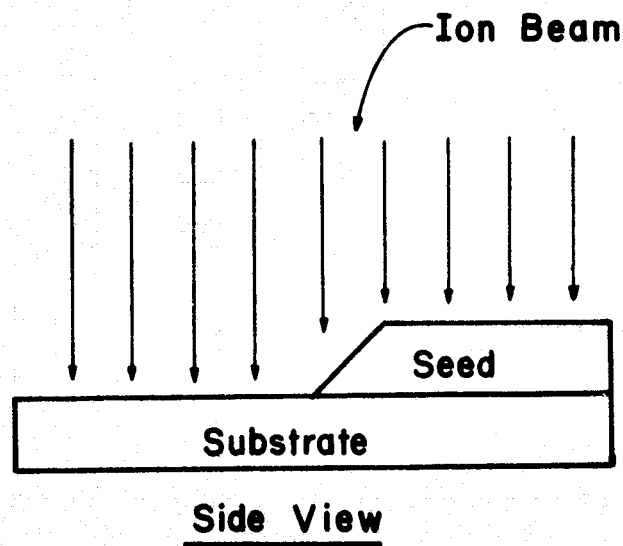
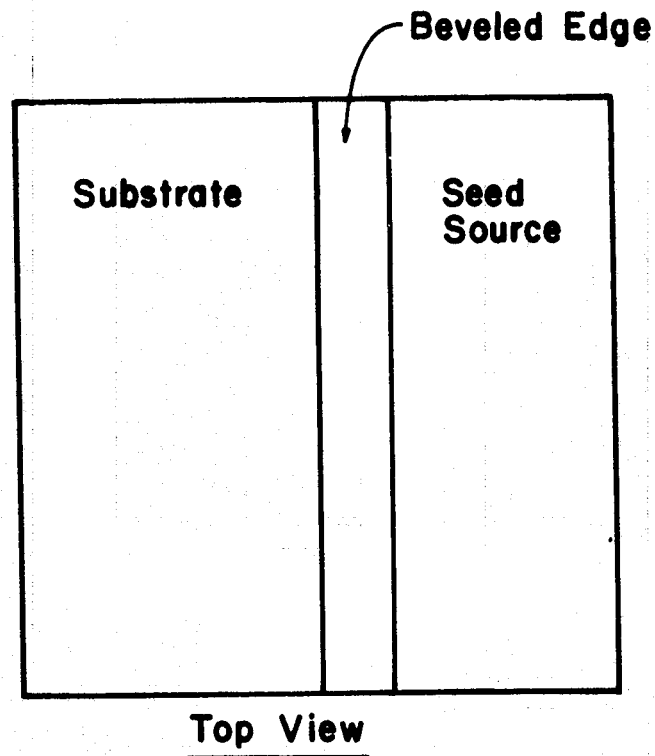


Fig. 3-1. Experimental seeding arrangement for ion beam texturing.

ORIGINAL PAGE IS  
OF POOR QUALITY

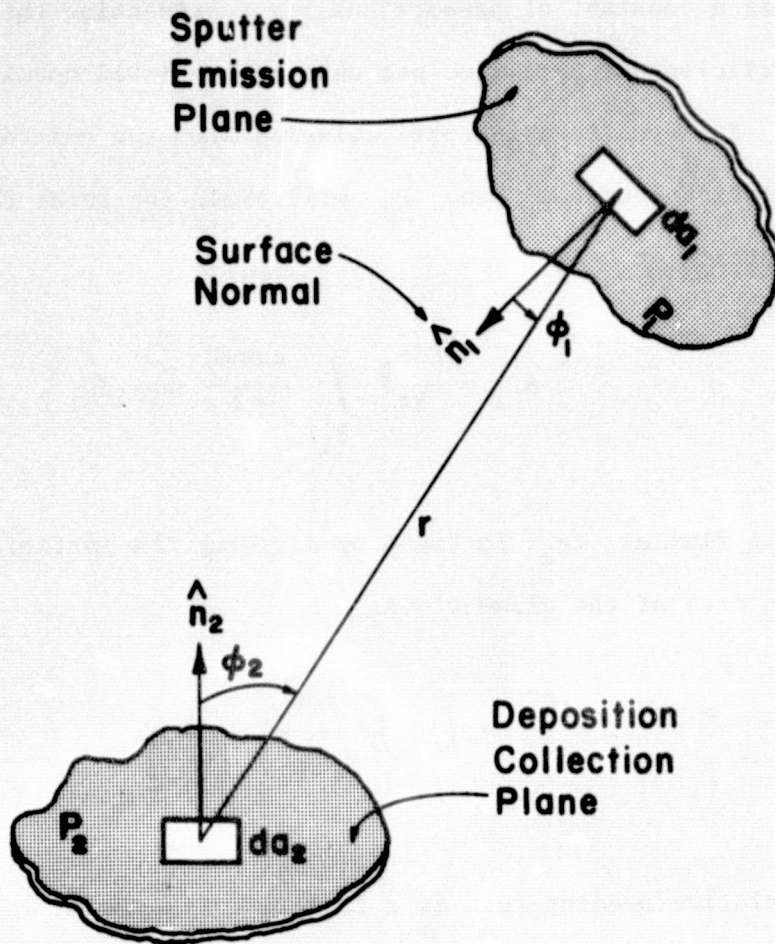


Fig. 3-2. Geometry for sputter emission and flux collection.

$$d\Gamma_2 = F da_1 \cos\phi_1 \frac{da_2 \cos\phi_2}{2\pi r^2} \quad (3-1)$$

where  $F$  is a constant of proportionality representing the sputtered flux in particles per unit time per unit area emitted normal to  $da_1$ . The factor  $F$  normalizes to total emission from the emitter plane,  $P_1$ .

Integrating over the plane  $P_1$  will yield the total rate of particle collection at  $da_2$

$$d\Gamma_2 = \frac{F da_2}{2\pi} \int_{P_1} \frac{\cos\phi_2}{r^2} \cos\phi_1 da_1 \quad (3-2)$$

An effective flux at  $da_2$  is found by dividing the particle arrival rate by the area of the element  $da_2$

$$F_2 = \frac{d\Gamma_2}{da_2} = \frac{F}{2\pi} \int_{P_1} \frac{\cos\phi_2}{r^2} \cos\phi_1 da_1 \quad (3-3)$$

The relative seeding rate as a function of position on the substrate plane can thus be found from the integral indicated in Eq. (3-3). This integral will, in general, not be solvable in closed form and will thus require a numerical procedure for evaluation.

Figure 3-3 shows the geometry and definition of variables to be used in a numerical integration algorithm. From Fig. 3-3 it can be seen that:

$$r^2 = (x_2 - x_1)^2 + y_1^2 \sin^2 \beta + (y_2 + y_1 \cos \beta)^2, \quad (3-4)$$



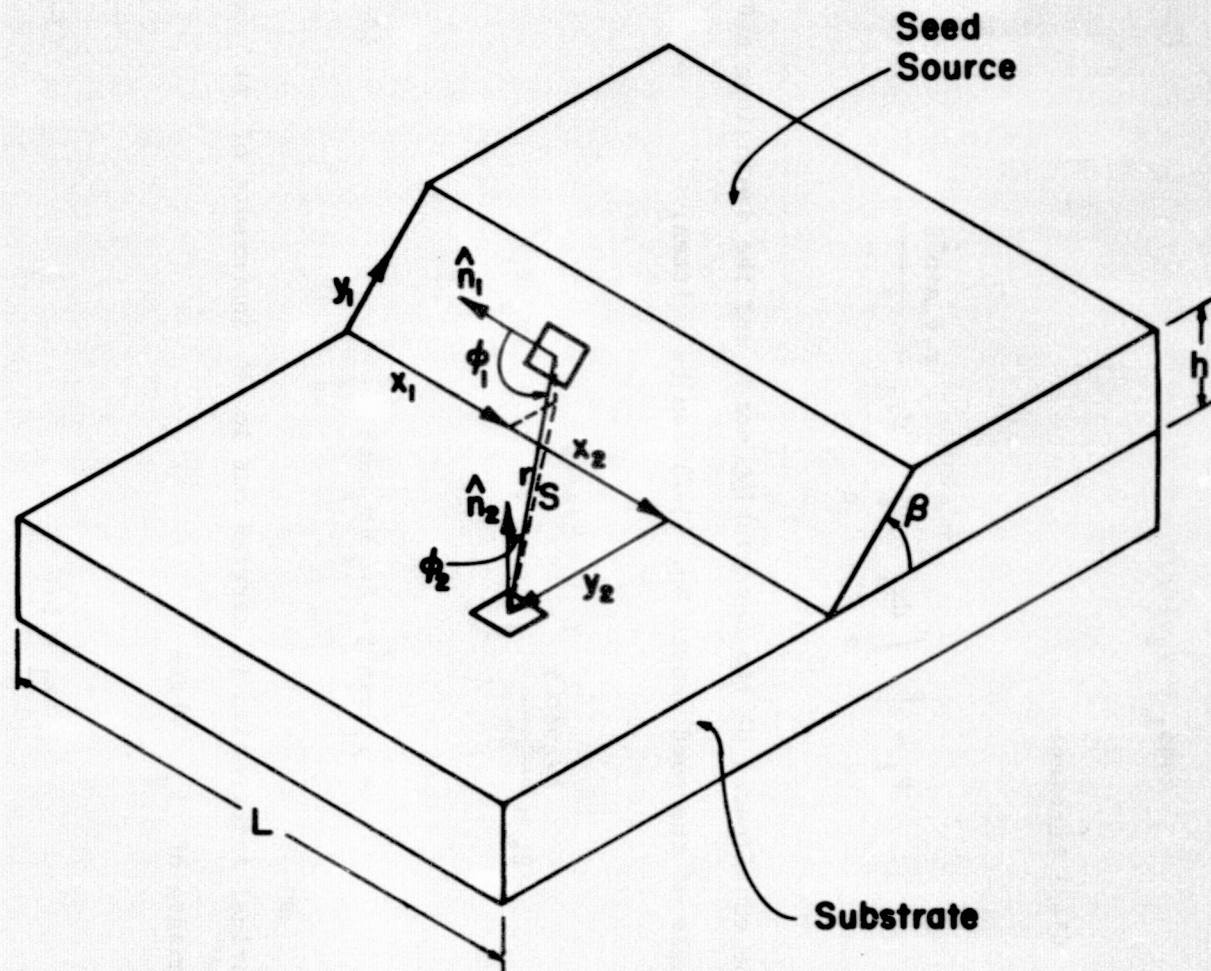


Fig. 3-3. Geometry and parameter definition for numerical integration algorithm.



$$\cos\phi_2 = y_1 \sin\beta / r , \quad (3-5)$$

and that

$$\cos\phi_1 = y_2 \sin\beta / r . \quad (3-6)$$

Thus Eq. (3-3) becomes:

$$F_2 = \frac{F}{2\pi} \int_0^L dx_1 \int_0^{h/\sin\beta} dy_1 \frac{y_1 y_2 \sin^2\beta}{r^4} . \quad (3-7)$$

Given the coordinates of the observation point and the dimensions and bevel angle of the seed source Eq. (3-7) can be written:

$$F_2 = \frac{F y_2 \sin^2\beta}{2\pi} \int_0^L dx_1 \int_0^{h/\sin\beta} dy_1 y_1 \left[ (x_2 - x_1)^2 + y_1^2 \sin^2\beta + (y_2 + y_1 \cos\beta)^2 \right]^{-2} . \quad (3-8)$$

The numerical integration is carried out in N increments of  $\Delta x$ , and M increments of  $\Delta y$ , where:

$$\Delta x_1 = L/N \quad (3-9)$$

and

$$\Delta y_1 = h/M \sin\beta . \quad (3-10)$$

The integral can now be written approximately as a summation:

$$\frac{F_2}{F} = \frac{y_2 \sin^2 \beta}{2\pi} \sum_{i=1}^N \sum_{j=1}^M \frac{\Delta x_1 \Delta y_1 y_{1j}}{\left[ (x_2 - x_{1i})^2 + y_{1j}^2 \sin^2 \beta + (y_2 + y_{1j} \cos \beta)^2 \right]^2} \quad (3-11)$$

where

$$x_{1i} = (i - \frac{1}{2}) \Delta x_1 \quad (3-12)$$

and

$$y_{1j} = (j - \frac{1}{2}) \Delta y_1 \quad (3-13)$$

A program was written to carry out the numerical procedure indicated in Eq. (3-11). The factor  $F$  is carried as a constant through the numerical work. It is, however, proportional to the ion arrival rate and the sputter yield of the seed material.

$$F = R_i \cos \beta Y(\beta) \quad (3-14)$$

where  $R_i$  is the ion arrival rate in ions per unit area per unit time at the substrate, the cosine of  $\beta$  takes into account the tilt of the beveled edge with respect to the ion beam direction, and  $Y(\beta)$  is the sputter yield of the seed material at the angle  $\beta$  in atoms per ion.

First, the integration step size necessary to assure convergence within one percent was investigated. The parameters used corresponded to a realistic experimental arrangement:  $L/h = 8.0$ ,  $\beta = 45^\circ$ ,  $x_2/h = 4.0$ , and  $y_2/h = 1.0$ . The results of calculating  $F_2/F$  as a function of  $N$  and  $M$  are given in Table 3-1.

Table 3-1. Integrations with Various Increments of Area

N	M	$F_2/F$
6	1	$3.0645 \times 10^{-2}$
11	2	$2.8013 \times 10^{-2}$
17	3	$2.6867 \times 10^{-2}$
23	4	$2.6396 \times 10^{-2}$
28	5	$2.6164 \times 10^{-2}$
34	6	$2.6035 \times 10^{-2}$
40	7	$2.5955 \times 10^{-2}$
45	8	$2.5903 \times 10^{-2}$
51	9	$2.5867 \times 10^{-2}$
154	27	$2.5746 \times 10^{-2}$
20	7	$2.5957 \times 10^{-2}$
10	7	$2.5948 \times 10^{-2}$
8	7	$2.5881 \times 10^{-2}$
6	7	$2.5489 \times 10^{-2}$
4	7	$2.3271 \times 10^{-2}$

Letting the  $N=154$ ,  $M=27$  value be the standard, this standard is approached within 1% by letting  $N=40$  and  $M=7$ . However,  $N$  can be further reduced by a factor of 4 without sacrificing significant accuracy. These values,  $N=10$  and  $M=7$ , are appropriate when the observation point  $y_2/h$  is a unit distance, or greater, from the source.

If  $y_2/h$  is decreased by a factor of two, accuracy can be maintained by increasing both  $M$  and  $N$  each by a factor of two. Other, similar adjustments would be appropriate as  $y_2/h$  changes.

The seeding rate variation as a function of distance from the center of the seed source is given in Table 3-2 for the choice of parameters:  $L/h = 8.0$ ,  $\beta = 45^\circ$ ,  $x_2/h = 4.0$ .

The data of Table 3-2 are plotted in Figs. 3-4 and 3-5. The seeding rate decreases rapidly near the source and falls off more slowly at greater distances as shown in Fig. 3-4. For typical dimensions of seed source and substrate, the seeding rate can vary by one or two orders of magnitude over the substrate. Both seeding rate and distance are represented on logarithmic scales in Fig. 3-5. The linear portion at large distances from the source has a slope corresponding to an inverse cubic variation with distance in agreement with the  $y_2$  dependence of Eq. (3-8). At small distances from the source, the seeding rate approaches a limiting value that would correspond to the seeding rate from a source of semi-infinite extent tilted at an angle  $\beta$ .

The limit can be calculated by integrating Eq. (3-8) after changing to suitable dimensionless variables:  $u = x_1/y_2$  and  $v = y_1/y_2$ .

$$(F_2/F)_{\text{limit}} = \frac{\sin^2 \beta}{2\pi} \int_{-\infty}^{\infty} du \int_0^{\infty} dv \, v \left[ u^2 + v^2 \sin^2 \beta + (1 + v \cos \beta)^2 \right]^{-2} \quad (3-15)$$

Equation (3-15) can be integrated to yield:

$$(F_2/F)_{\text{limit}} = (1 - \cos \beta)/4 \quad (3-16)$$

Table 3-2. Seeding Rate Along the Centerline of the Source.

$y_2/h$	$F_2/F$	$y_2/h$	$F_2/F$
0.03125	$7.07 \times 10^{-2}$	2.6	$8.02 \times 10^{-3}$
0.0625	$6.81 \times 10^{-2}$	2.7	$7.55 \times 10^{-3}$
0.125	$6.32 \times 10^{-2}$	2.8	$7.11 \times 10^{-3}$
0.5	$4.18 \times 10^{-2}$	2.9	$6.71 \times 10^{-3}$
0.6	$3.77 \times 10^{-2}$	3.0	$6.33 \times 10^{-3}$
0.7	$3.41 \times 10^{-2}$	3.1	$5.98 \times 10^{-3}$
0.8	$3.10 \times 10^{-2}$	3.2	$5.66 \times 10^{-3}$
0.9	$2.82 \times 10^{-2}$	3.4	$5.07 \times 10^{-3}$
1.0	$2.59 \times 10^{-2}$	3.5	$4.81 \times 10^{-3}$
1.1	$2.38 \times 10^{-2}$	3.6	$4.57 \times 10^{-3}$
1.2	$2.18 \times 10^{-2}$	3.7	$4.34 \times 10^{-3}$
1.3	$2.01 \times 10^{-2}$	3.8	$4.12 \times 10^{-3}$
1.4	$1.85 \times 10^{-2}$	3.9	$3.92 \times 10^{-3}$
1.5	$1.71 \times 10^{-2}$	4.0	$3.73 \times 10^{-3}$
1.6	$1.58 \times 10^{-2}$	8.0	$8.70 \times 10^{-4}$
1.7	$1.47 \times 10^{-2}$	16	$1.37 \times 10^{-4}$
1.8	$1.37 \times 10^{-2}$	32	$1.83 \times 10^{-5}$
1.9	$1.27 \times 10^{-2}$	64	$2.35 \times 10^{-6}$
2.0	$1.19 \times 10^{-2}$	128	$2.99 \times 10^{-7}$
2.1	$1.11 \times 10^{-2}$	256	$3.77 \times 10^{-8}$
2.2	$1.04 \times 10^{-2}$	512	$4.72 \times 10^{-9}$
2.3	$9.70 \times 10^{-3}$	1024	$5.92 \times 10^{-10}$
2.4	$9.09 \times 10^{-3}$	2048	$7.40 \times 10^{-11}$
2.5	$8.54 \times 10^{-3}$	4096	$9.26 \times 10^{-12}$

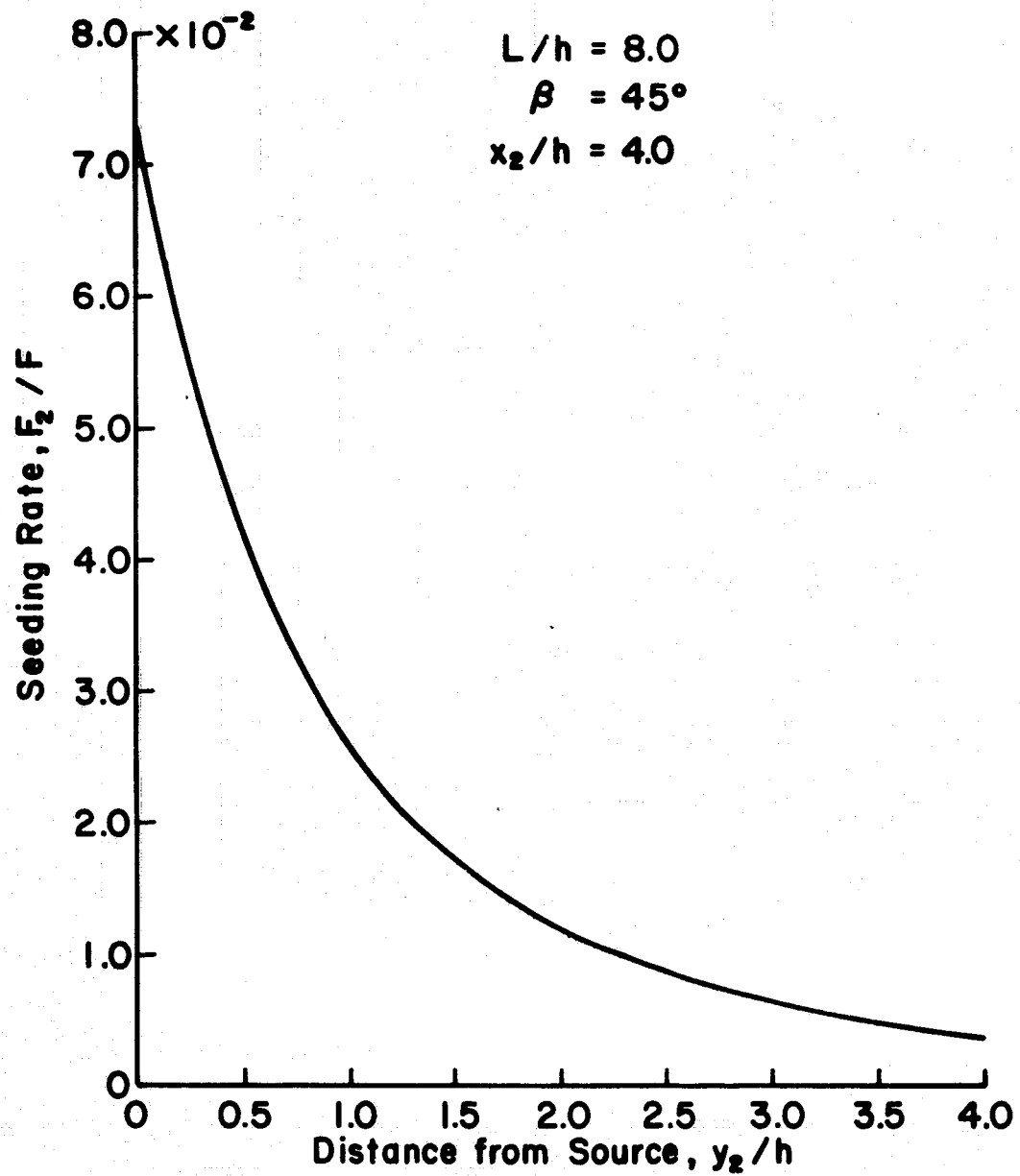


Fig. 3-4. Seeding rate versus distance from the seed source along the centerline.

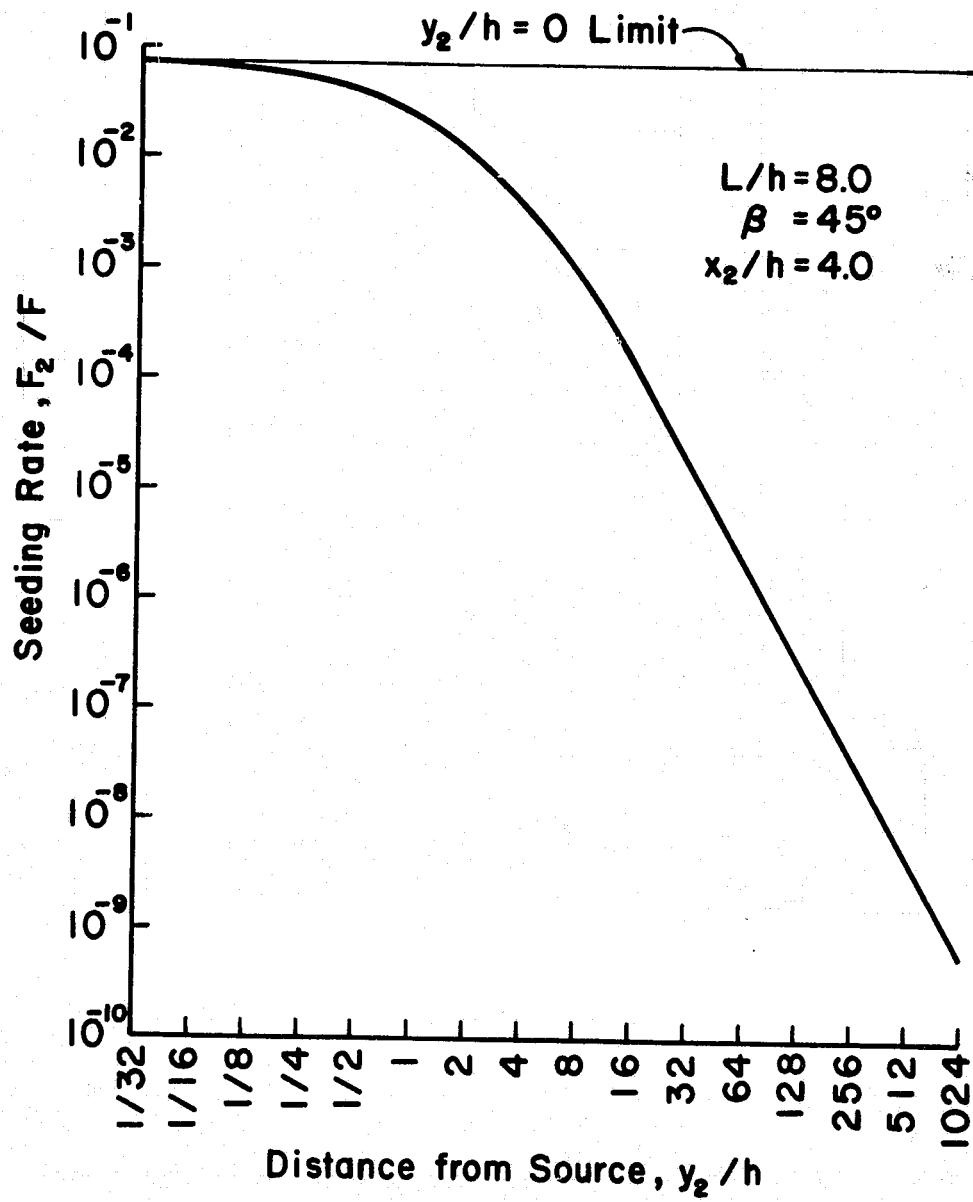


Fig. 3-5. Seeding rate versus distance from the seed source along the centerline (log-log plot).

which can be evaluated for  $\beta = 45^\circ$  as  $7.32 \times 10^{-2}$ . This value is plotted in Fig. 3-5 as the  $y_2/h = 0$  limit which the function approaches very closely at small  $y_2/h$ .

Table 3-3 lists calculated values for  $F_2/F$  obtained over a regular mesh covering the substrate region for the same geometrical parameters used for Table 3-2. The data of Table 3-3 are plotted in Fig. 3-6. Close to the seed source there is a strong variation with lateral position dropping to only about one half the center value at the extreme ends where flux contributions are being received from the right or left side only. As the observation line is moved further from the source the lateral variations diminish considerably because the subtended angle of the seed source is then changed less when observed from various lateral positions.

An Auger surface composition analysis done at various distances from the shield location on a seeded sample should provide an experimental verification of the calculated profile shown in Fig. 3-4.

From seeding theory (see Section II) we have shown that the critical temperature varies inversely as the logarithm of the seeding density times a constant.

$$T_c \approx \frac{E_d \cdot 11600^\circ K}{25 + \ln F_s} \quad (3-17)$$

for reasonable magnitudes of the variables ( $E_d$  in eV). Table 3-4 shows a possible variation of  $T_c$  with  $F_s$ .



Table 3-3. Calculated Values for  $F_2/F$  for Positions on the Substrate.

$x_2/h$	$y_2/h$							
	0.5		1.0		1.5		2.0	
0.0	2.11	$10^{-2}$	1.33	$10^{-2}$	8.92	$10^{-3}$	6.35	$10^{-3}$
0.5	3.32	$10^{-2}$	1.86	$10^{-2}$	1.16	$10^{-2}$	7.89	$10^{-3}$
1.0	3.82	$10^{-2}$	2.20	$10^{-2}$	1.37	$10^{-2}$	9.20	$10^{-3}$
1.5	4.02	$10^{-2}$	2.39	$10^{-2}$	1.51	$10^{-2}$	1.02	$10^{-2}$
2.0	4.11	$10^{-2}$	2.49	$10^{-2}$	1.60	$10^{-2}$	1.09	$10^{-2}$
2.5	4.15	$10^{-2}$	2.55	$10^{-2}$	1.66	$10^{-2}$	1.14	$10^{-2}$
3.0	4.17	$10^{-2}$	2.58	$10^{-2}$	1.69	$10^{-2}$	1.17	$10^{-2}$
3.5	4.18	$10^{-2}$	2.59	$10^{-2}$	1.71	$10^{-2}$	1.18	$10^{-2}$
4.0	4.18	$10^{-2}$	2.59	$10^{-2}$	1.71	$10^{-2}$	1.19	$10^{-2}$

$x_2/h$	$y_2/h$							
	2.5		3.0		3.5		4.0	
0.0	4.72	$10^{-3}$	3.62	$10^{-3}$	2.85	$10^{-3}$	2.29	$10^{-3}$
0.5	5.67	$10^{-3}$	4.25	$10^{-3}$	3.28	$10^{-3}$	2.60	$10^{-3}$
1.0	6.53	$10^{-3}$	4.83	$10^{-3}$	3.69	$10^{-3}$	2.89	$10^{-3}$
1.5	7.22	$10^{-3}$	5.32	$10^{-3}$	4.04	$10^{-3}$	3.14	$10^{-3}$
2.0	7.75	$10^{-3}$	5.70	$10^{-3}$	4.32	$10^{-3}$	3.35	$10^{-3}$
2.5	8.12	$10^{-3}$	5.99	$10^{-3}$	4.54	$10^{-3}$	3.52	$10^{-3}$
3.0	8.36	$10^{-3}$	6.18	$10^{-3}$	4.69	$10^{-3}$	3.64	$10^{-3}$
3.5	8.49	$10^{-3}$	6.30	$10^{-3}$	4.78	$10^{-3}$	3.71	$10^{-3}$
4.0	8.54	$10^{-3}$	6.33	$10^{-3}$	4.81	$10^{-3}$	3.73	$10^{-3}$

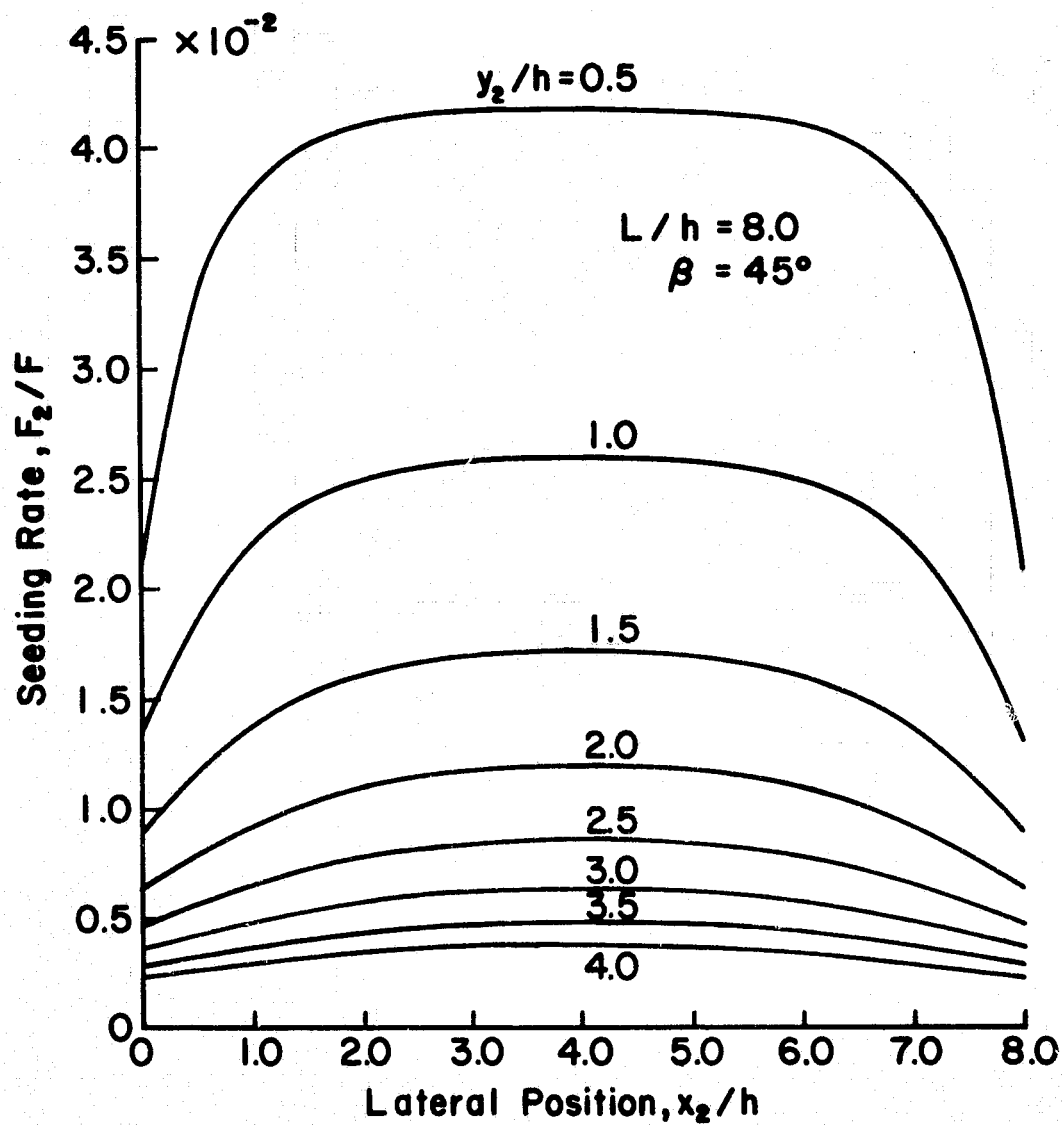


Fig. 3-6. Seed flux on lines parallel to the source at increasing distances from the source.

Table 3-4. Variation of Critical Temperature  
With Seed Fraction.

$T_c$	$F_s$	$\Delta T_c$
735°K	.0001	
641°K	.001	94°K
569°K	.01	72°K
511°K	.1	58°K
464°K	1.0	47°K

Thus, the variation in seeding density across a substrate can be translated into a corresponding variation in the critical texturing temperature across the substrate. Contours of equal critical temperature can in theory be specified as to shape and position. If a substrate were held at a temperature corresponding to a contour a certain distance from the seed source, then locations between the source and that contour would be textured and locations beyond would remain non-textured. Such a texture boundary would be convex, curved and symmetrical about the centerline of the seed source. Silicon seeded with Mo has exhibited textured regions suggestive of this effect.

The technique presented here for calculating seeding rate can be used to determine appropriate seed source geometries to be utilized when uniform seeding is desired over an entire substrate to generate uniform texturing.

#### IV. ENERGETIC BINARY COLLISIONS IN RARE GAS PLASMAS

Energetic binary collisions become important in plasmas where high voltages are introduced to accelerate ions toward a target or to form a beam. Interest in these collision cross sections arose primarily in connection with experimental work involving the propagation of ion beams used for sputtering and processes occurring within diode plasma sputtering devices.<sup>1,2</sup> Thus, although they should also be of interest in other areas, the cross sections obtained herein are largely described in terms of their impact on the understanding of these particular experimental sputtering applications as representative systems. Energies of several hundred eV are typically employed in diode sputtering and in ion beam devices.<sup>3</sup> At such energies, interaction cross sections differ sharply from their values at very low or thermal energies.<sup>4</sup>

The plasmas and beams generated in sputtering devices are typically derived from rare gases with Ar by far being the most common. Other more reactive gases are employed occasionally to achieve special effects due to chemical reactions. This work is restricted to consideration of Ar, Kr, and Xe for momentum and energy transfer calculations.

While it is recognized that electrons will generally be present in plasmas and propagating beams, their collisional effects will be neglected. Electrons are important in plasmas and ion beams for space-charge neutralization and for current neutralization of an ion beam, but do not otherwise enter significantly into reactions with high energy ions. Electron masses are on the order of  $10^{-5}$  of atom masses so that energy and momentum losses to electrons are negligible. The process of recombination of electrons with ions can likewise be

neglected because the cross section for this process is several orders of magnitude smaller than other cross sections of interest.<sup>5</sup>

Work on these interaction cross sections was begun during the previous support period.<sup>6</sup> The work on resonance charge exchange will not be repeated here nor will the details of the calculation techniques. The collision cross sections reported earlier however, dealt only with Ar and only with the cross section for directed momentum loss. Additional cross sections for Kr and Xe have been calculated and two types of total cross sections have been addressed: momentum transfer and energy transfer, corresponding to the customary diffusion and viscosity cross sections respectively.

#### Elastic Collision Dynamics

Only through scattering from particles of comparable mass can energetic particles lose both significant energy and forward momentum. This study involves, specifically, elastic collisions between like neutral particles, but the qualitative trends may be useful in understanding ion-atom collisions or unlike atom collisions as well. The probability of charge exchange prior to elastic collisions is high for beam ions. Thus, the collision of high velocity neutrals with low velocity neutrals is the dominant process for momentum and energy loss by beam particles prior to sputtering.

The deBroglie wavelength of an Ar, Kr, or Xe atom at typical ion energies is very small compared to atomic dimensions, allowing the use of classical particle trajectories as a first approximation to the scattering.

If the interaction potential between two atoms is known, the classical equations of motion can be solved to relate the scattering angle

to the impact parameter for the incident atom. The solution is most directly obtained using center of mass coordinates where a particle of reduced mass  $\mu$  interacts with a fixed center of force through a potential  $V(r)$  where  $r$  is the separation distance of the particle from the center of force.<sup>7</sup> Solving the equation of motion yields an expression for the scattering angle in the laboratory frame of reference<sup>7,8</sup>

$$\theta = 2\pi - 4s \int_{r_0}^{\infty} \frac{dr}{r^2} \left( 1 - \frac{s^2}{r^2} - \frac{V(r)}{\frac{1}{2}\mu v_0^2} \right)^{-\frac{1}{2}} \quad (4-1)$$

where  $v_0$  is the speed of the incident particle,  $s$  is the impact parameter, and  $r_0$  is the distance of closest approach.

The integration of Eq. (4-1) is not straightforward because the upper limit is infinite and the integrand itself has a singularity at the point of closest approach. Closed form solutions in terms of elliptic integrals are known for only a few power-law functions of  $r$  for the potential  $V(r)$ .<sup>7</sup> The actual integration can be carried out numerically after a change of variables to  $u = 1/r$  which gives finite limits but does not remove the singularity in the integral. An algorithm was developed for this integration utilizing a ten-point Gauss-Legendre quadrature scheme along with a logarithmically decreasing integration interval as the integration proceeds from the well-behaved end of the interval toward the singularity. Before integrating, the upper limit of integration,  $u_0 = 1/r_0$ , was first determined by an iterative solution to the (usually) transcendental equation:

$$2V(r_0)/E_t + s^2/r_0^2 = 1 \quad (4-2)$$

where  $E_t$  is the energy of the incident particle in the laboratory frame of reference.

To verify that the integration algorithm was functioning properly, scattering angles for an inverse square law force (Rutherford Scattering) were calculated. These calculated angles were compared with the closed-form solution and the numerical values exhibit a divergence of only a few units in the third significant figure.

#### Interaction Potentials

To use a classical approximation for potential scattering it is necessary to obtain a potential function describing the pair interaction. Barker, Fisher and Watts<sup>9</sup> have developed an Ar pair potential that is recognized as being in best overall agreement with experimental data from a number of sources such as specific heats, internal energies, viscosities, solid state parameters, and scattering data. Barker et. al.<sup>10</sup> have developed potentials for Kr and Xe using nearly the same analytical form for the potential as for Ar with similar adjustable parameters.

The screened Coulomb potential used by Bingham<sup>11</sup> and Everhart et. al.<sup>12,13</sup> is valid at higher energies (e.g., above 50KeV) but disregards the electron repulsion important at lower energies. Smoothly joining the Bingham<sup>11</sup> and Barker<sup>9</sup> potentials between the energies where each potential is known to fit experimental data well, supports the use of Barker's results up to about 1KeV.

Figure 4-1 compares the pair potentials used for Ar, Kr and Xe showing the increase in effective radius of the atom as the atomic number increases. The general character of the like-particle scattering from Kr and Xe in the classical approximation should be similar to Ar since the potential shapes are similar to Ar. However, the corresponding cross sections for the heavier gases should be larger at the same collision energy.

#### Calculated Cross Sections

Numerical solutions to Eq. (4-1) allow the calculation of differential collision cross sections for different energies and gases. The differential cross section is given by<sup>7</sup>

$$\sigma(\theta) = - \frac{s}{\sin\theta} \frac{ds}{d\theta} . \quad (4-3)$$

In a collision in which an atom is scattered through an angle  $\theta$ , it will have lost a fraction of its energy equal to  $(1-\cos^2\theta)$ . Integrating this fraction weighted by the differential cross section gives the customary form for the widely used cross section for viscosity<sup>14</sup>

$$Q_E = \int_0^{\pi/2} (1-\cos^2\theta) \sigma(\theta) 2\pi\sin\theta d\theta . \quad (4-4)$$

A similar expression is obtained when the loss of total momentum is considered. This momentum loss cross section is used to describe diffusion processes.

$$Q_p = \int_0^{\pi/2} (1-\cos\theta) \sigma(\theta) 2\pi\sin\theta d\theta \quad (4-5)$$



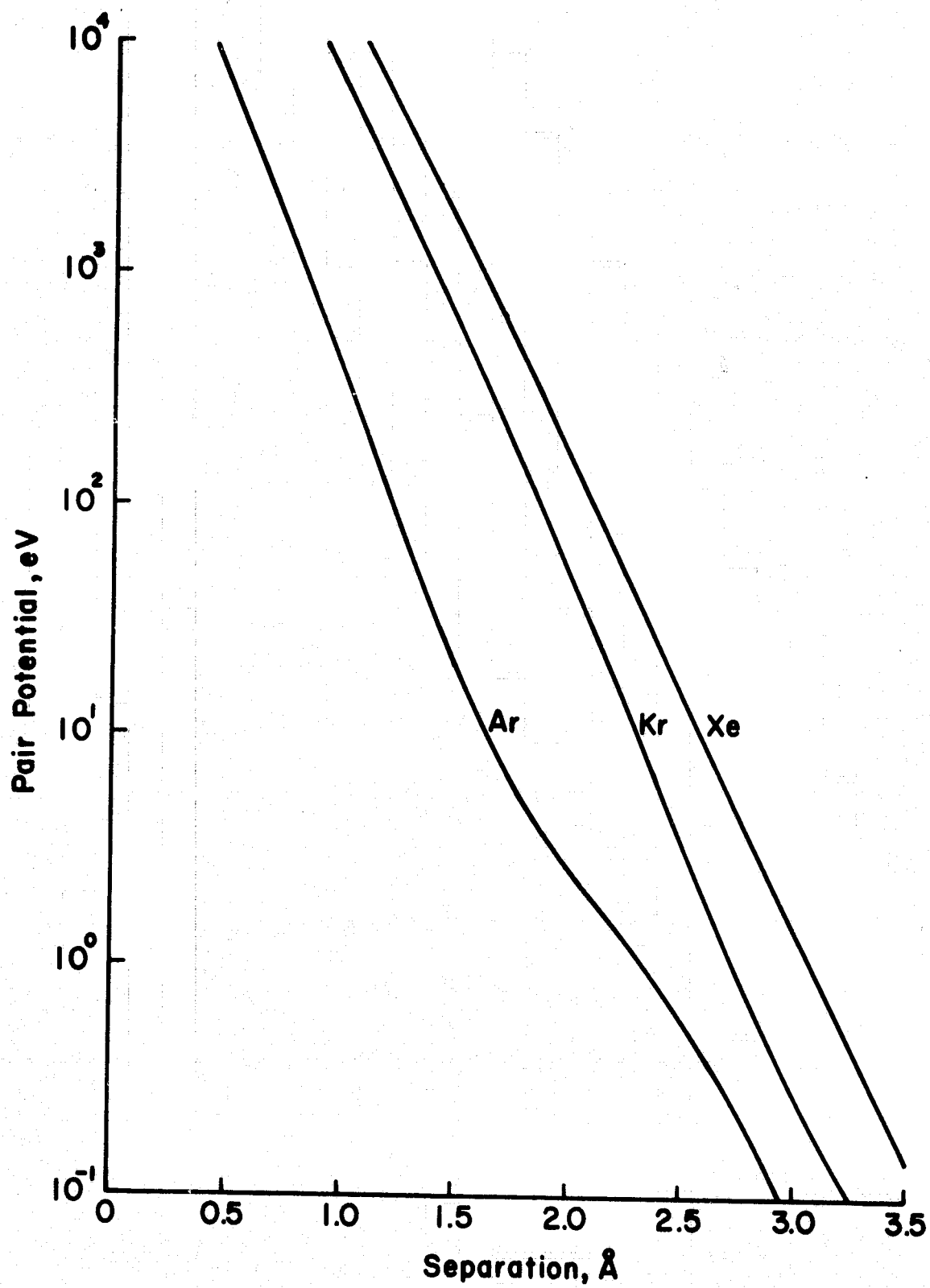


Fig. 4-1. Pair potentials for rare gases.

Integration of Eqs. (4-4) and (4-5) yields the total cross sections for energy and momentum transfer given in Table 4-1 and plotted in Fig. 4-2 and 4-3 over the energy range from 1eV to 1000eV.

### Conclusion

Rare gas interaction cross sections have been obtained that will allow a more thorough analysis and understanding of a variety of energetic processes involved in ion beam and plasma devices. Cross sections at these high energies have not previously been available to investigators, resulting in the occasional erroneous use of thermal values. The argon energy transfer cross section has been successfully applied to the elucidation, by Harper et. al.,<sup>4</sup> of a complex negative ion sputtering phenomenon discovered in a diode plasma device. These cross sections for elastic collision processes along with the charge exchange cross section allow designers of ion beam deposition and machining experiments to quickly arrive at appropriate geometries and pressure environments for beam propagation.

Table 4-1. Calculated Energy and Momentum Transfer Cross Sections.

Energy, eV	Energy Transfer Cross Section, Å <sup>2</sup>			Momentum Transfer Cross Section, Å <sup>2</sup>		
	Ar	Kr	Xe	Ar	Kr	Xe
1	11.2	14.0	17.7	7.17	9.04	11.5
2	9.54	12.5	15.9	6.07	8.10	10.3
3	8.57	11.8	14.9	5.42	7.61	9.66
5	7.37	10.9	13.8	4.63	7.03	8.93
10	5.88	9.78	12.4	3.68	6.31	8.02
20	4.72	8.77	11.1	2.97	5.66	7.18
30	4.20	8.22	10.4	2.65	5.30	6.73
50	3.67	7.55	9.59	2.32	4.86	6.17
100	3.09	6.70	8.51	1.96	4.30	5.47
200	2.60	5.89	7.49	1.65	3.77	4.81
300	2.34	5.44	6.93	1.48	3.48	4.44
500	2.03	4.89	6.24	1.28	3.12	3.99
1000	1.65	4.19	5.36	1.04	2.66	3.41

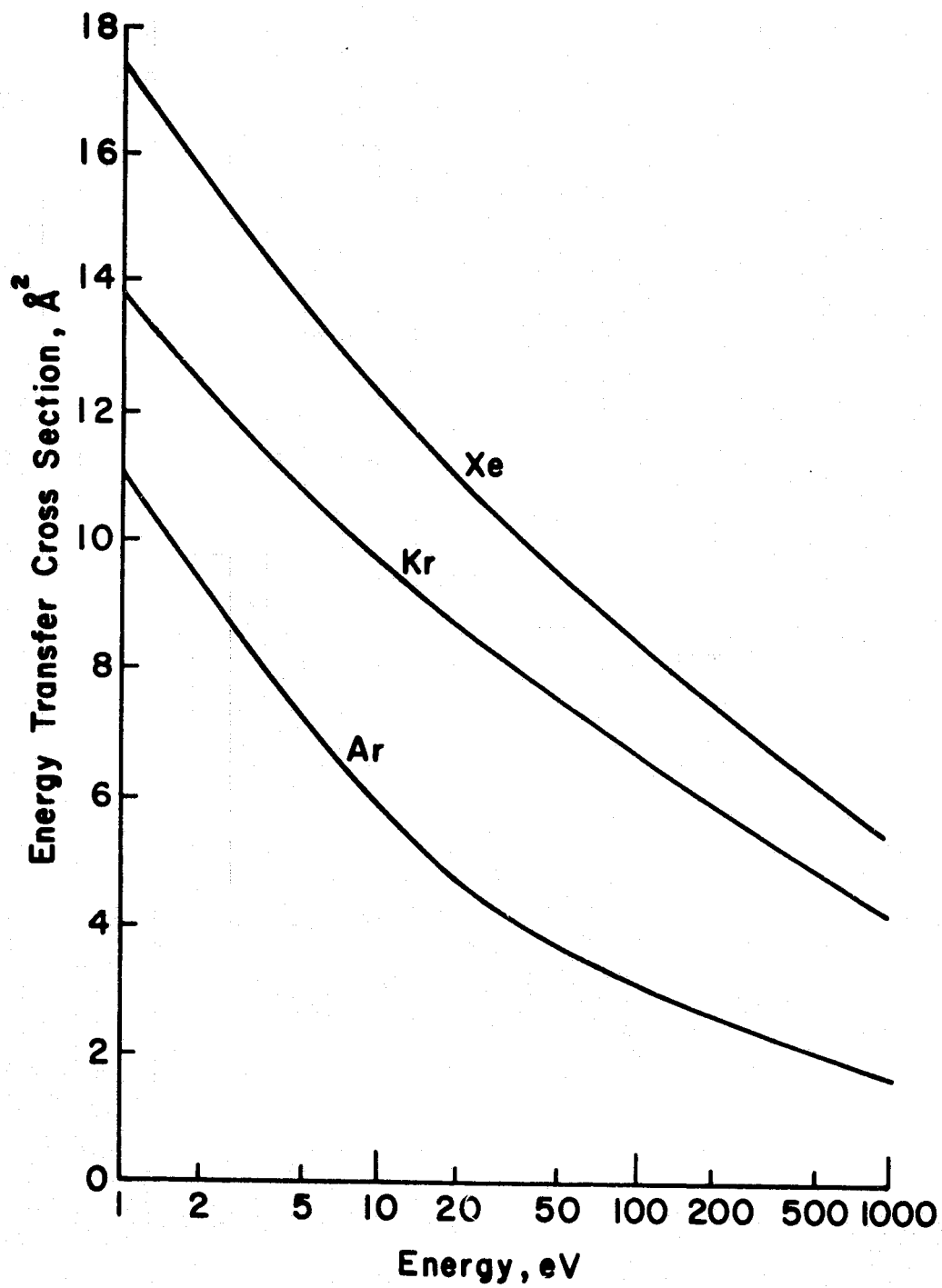


Fig. 4-2. Energy transfer (viscosity) cross section for Ar, Kr, and Xe as a function of energy.

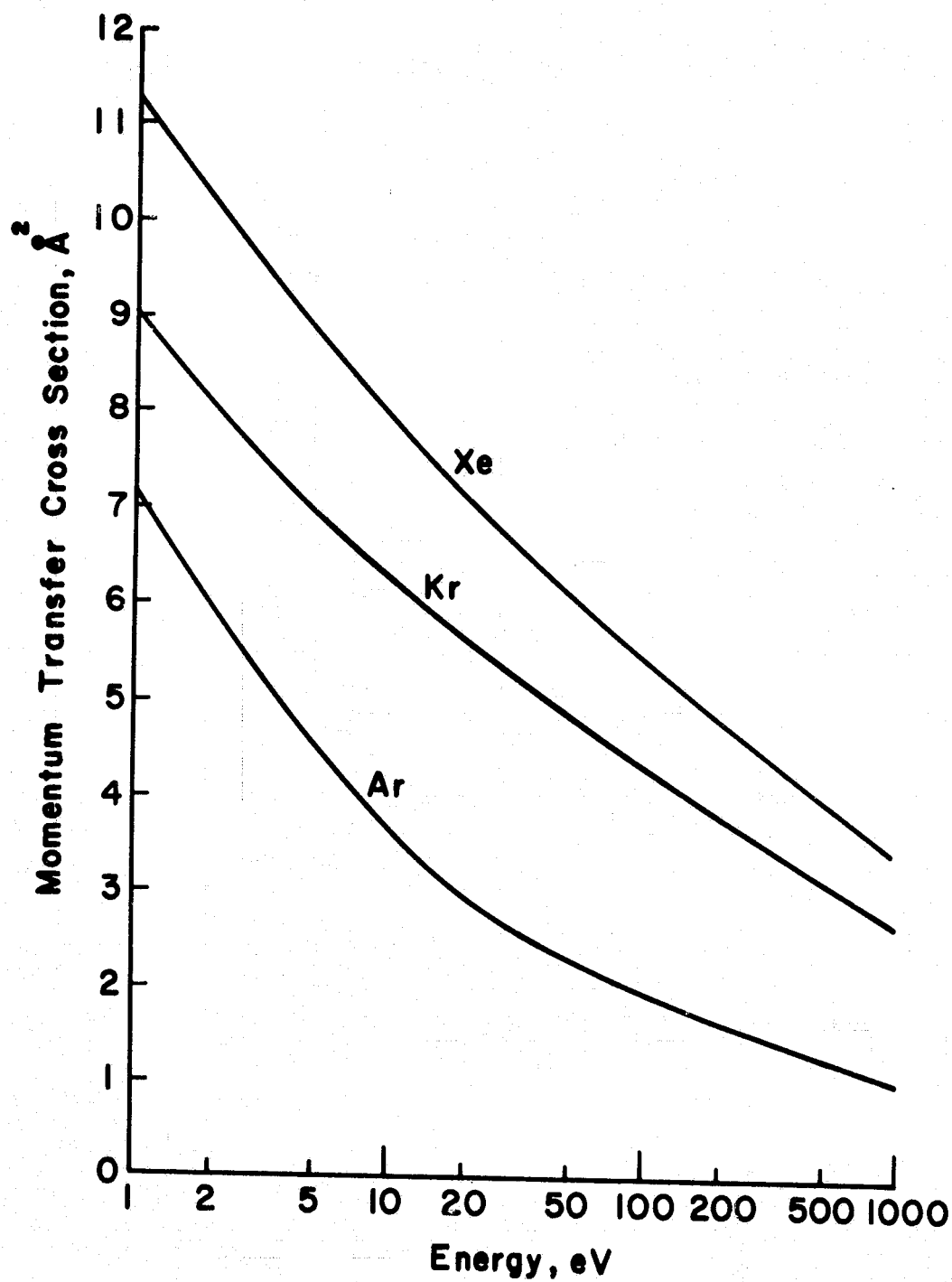


Fig. 4-3. Momentum transfer (diffusion) cross section for Ar, Kr, and Xe as a function of energy.

## V. PHYSICAL SPUTTERING AND REACTIVE ION ETCHING

by Curtis M. Haynes

Experiments in seeding and surface texturing have been performed with an Ar ion beam using various combinations of seed material and substrates. In addition, the characteristics of ion source operation with  $\text{CF}_4$  have been studied.

### Ion Source Operation with $\text{CF}_4$

A multipole ion source 7.6 cm in diameter and 5.1 cm long was tested using  $\text{CF}_4$  as the working gas. A refractory metal cathode was mounted in the center of the discharge chamber. A set of dished Mo grids was masked down to a beam diameter of 5 cm using 0.025 mm Ta foil.

This source was operated with both  $\text{CF}_4$  and Ar for comparison of operating conditions. Figure 5-1 is a plot of discharge loss per extracted beam ion as a function of total beam current. The  $\text{CF}_4$  discharge tended to extinguish at low discharge voltages so it was operated at 75 V while Ar discharges are typically 50 V. Comparisons were made at different pressures with the pressure being measured at the background pressure of the vacuum system and not inside the ion source itself. Neither gas gave a stable discharge below about  $1 \times 10^{-4}$  Torr. From Fig. 5-1 it can be seen that the power requirements for  $\text{CF}_4$  are about 50 percent greater than for Ar for the same beam current.

Looking at discharge current alone rather than discharge power (Fig. 5-2) it can be seen that the ratio of discharge current to beam

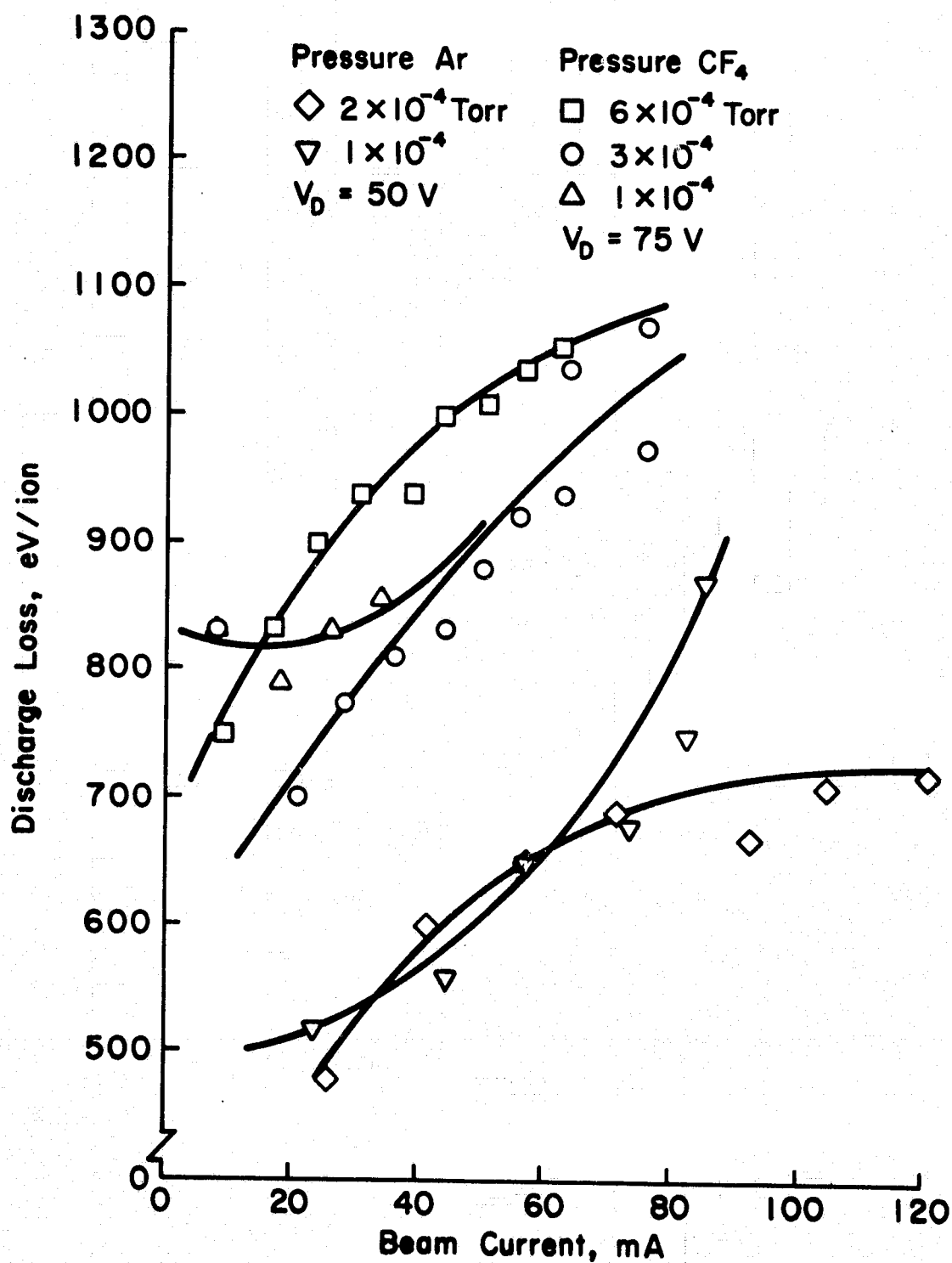


Fig. 5-1. Comparison of Ar and CF<sub>4</sub> source operating characteristics.

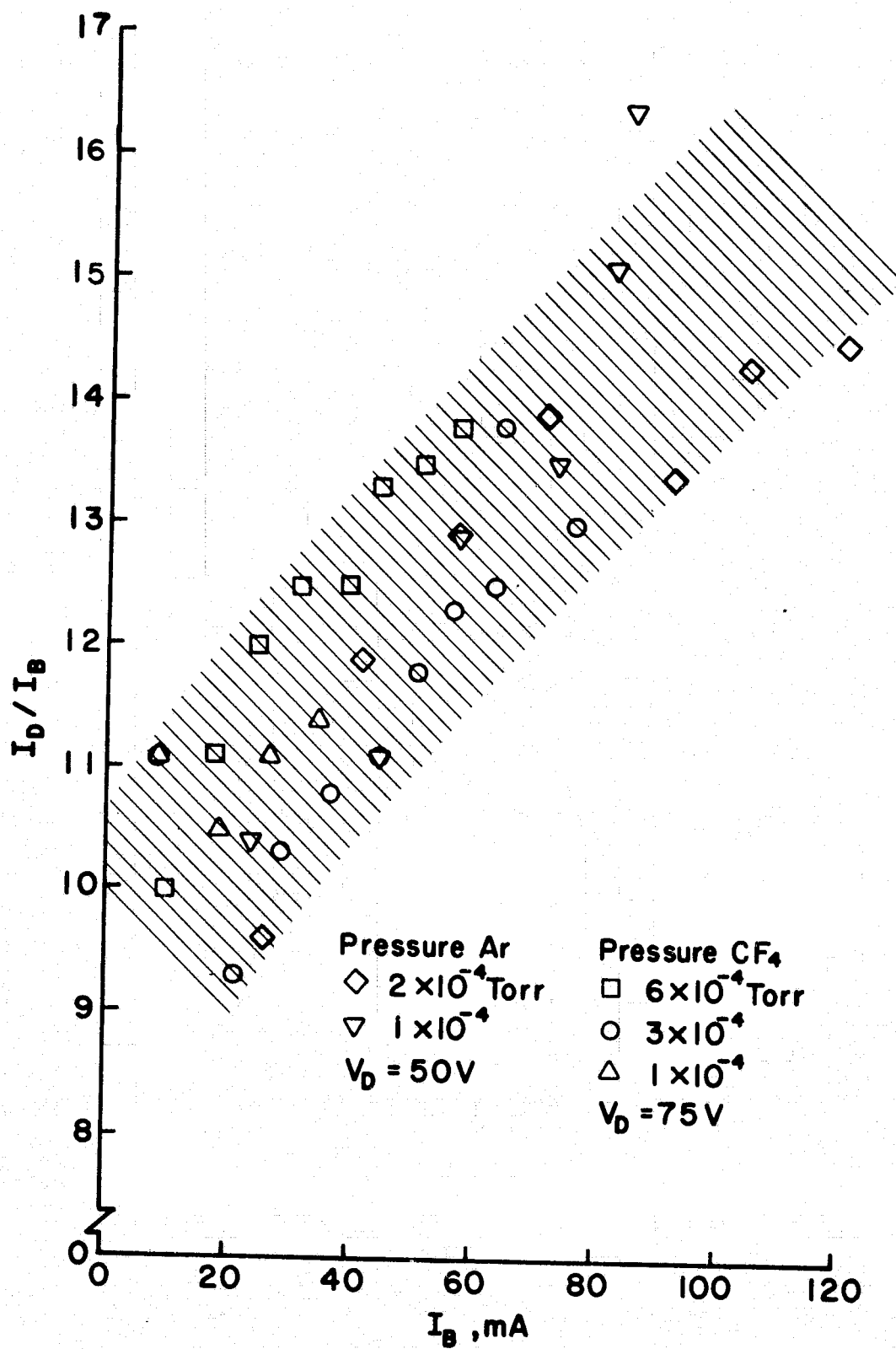


Fig. 5-2. Correlation for Ar and  $\text{CF}_4$  source operation.



current correlates approximately linearly with beam current for both working gases.

If the source is operated using  $\text{CF}_4$  with a constant cathode heater current there is a steady decrease in discharge current with source operation becoming impossible within about three hours. This reduction in discharge current is felt to be the result of a slow buildup of a non-conducting layer on the anodes, and a contributor to the data scatter in Fig. 5-1. The Ta cathode is also degraded by operation with  $\text{CF}_4$ , becoming white and brittle within less than one hour of discharge operation. The 0.025 mm Ta foil used to mask the grids was eroded completely through with about ten hours total of  $\text{CF}_4$  discharge operation. In contrast, Ar used in the chamber for over 30 hours did not cause measurable erosion damage to the foil.

Differences in the physical appearance of the interior of the discharge chamber were noticed after using each of three different propellants. When operated with Hg the stainless steel surfaces developed a very shiny appearance that lasted through months of storage. In addition, the Fe pole pieces did not show any evidence of corrosion, whereas pole pieces that were made at the same time but never used inside a discharge chamber developed a layer of rust in the same storage environment. When operated with Ar, the interior surfaces lost their shine and became a light, dull gray. Finally, a darker gray coating is observed after  $\text{CF}_4$  operation.

#### Seeding and Texturing Experiments

A variety of seeding and texturing experiments were done using a 500eV  $\text{Ar}^+$  ion beam. Unless otherwise specified, the beam current

density was set at  $1 \text{ mA/cm}^2$ . Substrates were sputtered while resting on a heater with the temperature monitored using a thermocouple.

### Aluminum

Al was sputtered at  $475^\circ\text{C}$  using Fe as a seed material. Experiments have been performed using Fe as both a seed material and as a substrate in attempts to observe ferromagnetic clustering phenomena made possible by surface diffusion. The only system so far to exhibit what are believed to be ferromagnetic effects is an Al substrate seeded with Fe. An array of long, narrow clusters of material could be seen with the long clusters preferentially aligned along what appear to be two mutually orthogonal directions (Fig. 5-3). It appears that the clusters might be ferromagnetic and aligned in preferred directions defined by the crystal planes of the underlying Al which has an fcc structure. It would seem reasonable that ferromagnetic coupling is responsible for the linear growth of the clusters because of the magnetic anisotropy that would be encountered by a diffusing Fe atom approaching a magnetized cluster.

In support of the hypothesis that these linear structures are aligned in some way with the underlying substrates, sharp boundaries could be located across which the direction of the alignment axes shifts. Figure 5-4 shows such a boundary where the axes exhibit a rotation of nearly  $20^\circ$  about the vertical after correction for the aspect of the micrograph.

Samples of high purity Al were obtained and sputtered. When compared with results obtained using Al of lesser (but uncertain) purity, no significant differences between the sputtered surfaces could be observed. Both types of Al, in the absence of deliberate seeding,

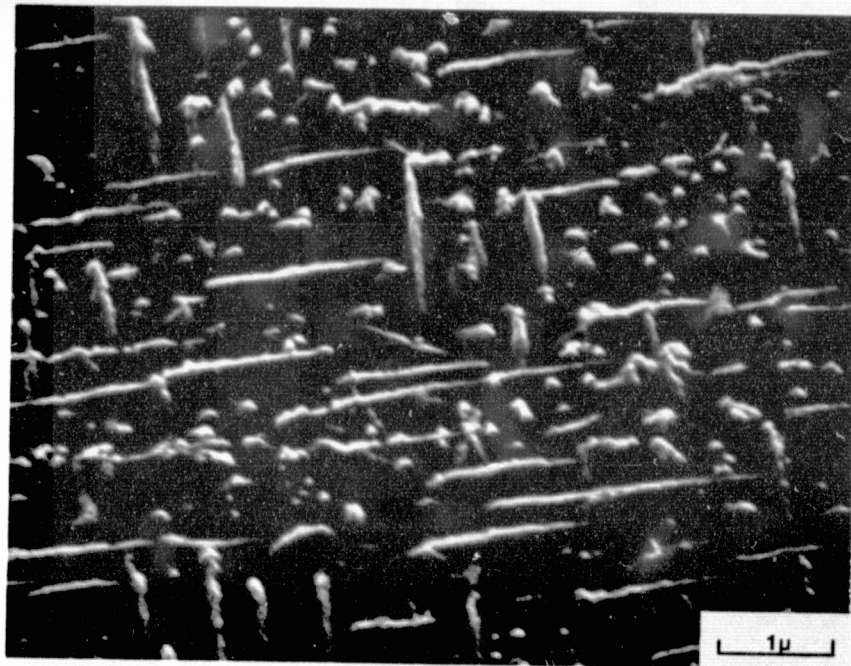


Fig. 5-3. Aluminum seeded with Fe.

ORIGINAL PAGE IS  
OF POOR QUALITY

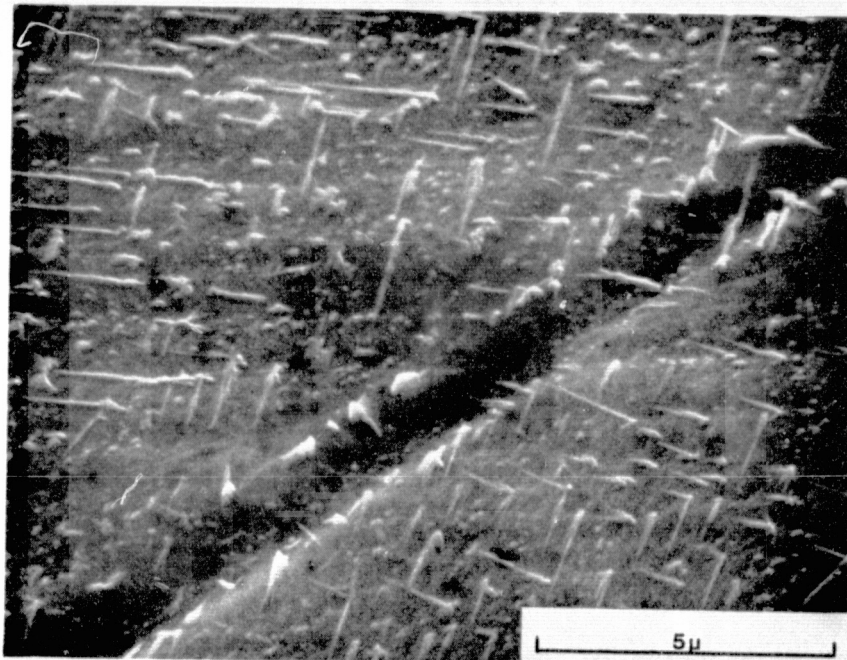


Fig. 5-4. Aluminum seeded with Fe, grain boundary.

developed undulating surfaces without a cone structure; however, small (several hundred Angstroms) bits of material can be seen widely scattered on the surface. These tend to be rounded and not cone-shaped. Possibly aluminum oxide is forming on the surface during sputtering or perhaps some other impurities are being deposited onto the surface.

No cones were formed when Al was seeded with Ta at 475°C.

### Graphite

Sputter time had the effect of increasing whisker density and size with increasing sputter time. C samples were sputtered for 5, 10 and 20 minute intervals and showed small whisker growth, no more than 0.5  $\mu$  in height. The etched surfaces, other than the whiskers, appeared slightly smoother than the non-sputtered portions of the C sample. Other sputter times of 1, 2, 4, and 8 hours showed a whisker length in approximate proportion to the sputter time. An increase in the diameter of individual whiskers with time was also observed along with a reduction in the areal density of whiskers. Total sputtering time appears to be the most significant factor in whisker growth.

Temperature was also a factor in whisker growth. Samples were sputtered for 1 and 4 hours at holder temperatures of approximately 15°C, 300°C and 500°C. All experiments showed a decrease in whisker growth with higher temperatures.

Two sets of samples were sputtered for 4 hours, one set with an ion beam neutralized using an immersed thermionic neutralizer and the other without neutralization. Various shield materials were used. All samples sputtered using a thermionically neutralized beam exhibited a greater density of whiskers that were also somewhat longer on the



average than those on corresponding samples sputtered with a non-neutralized ion beam.

Various shield geometries were compared: vertical edge, beveled edge up, beveled edge down, and circular cross section. The whiskers produced using a vertical shield edge or a shield with a beveled edge down tended to be small but uniform over the entire sample. However, near a shield of circular cross section or with the beveled edge up, the whiskers tended to cluster near the shield with a marked reduction in size and density further from the shield. With no shield the whiskers were uniformly distributed over the sample but were not generally as long or as dense as those closest to a beveled shield.

Two different types of commercially available graphite were also compared: Union Carbide grade ATJ and POCO Graphite. No differences in whisker growth were observed between the two types of graphite.

Qualitative x-ray fluorescence (an SEM attachment) and x-ray diffraction experiments were carried out to determine the composition of the C whiskers. A lattice spacing characteristic of the whiskers was 3.39 Å. The absence of other lines from the powder pattern was a further indication of graphite. X-ray fluorescence had indicated Fe in the whisker samples. Carbon is not detectable using that apparatus and similar levels of Fe signal were also found using samples that were believed to have very little Fe. The whiskers are thus felt to be mostly graphite.

Optical absorption measurements were taken of C whisker samples sputtered at an etch dose of 8 mA-hrs/cm<sup>2</sup>. At normal incidence and at a light source tilt of 64° from normal about 98.5% of the light from a wavelength of 3500 Å to about 17000 Å was absorbed. The absorption decreased to about 97% at 25000 Å.

### Silicon

After numerous attempts to texture Si with a variety of seed materials it was found that temperatures above 500°C were usually required. Polished, single-crystal Si wafers were sputtered at 500°C, 550°C and 600°C for 60 minutes. Half of the wafers were cut parallel to the (111) plane and half were cut parallel to the (100) plane. Both Au and Fe were used as seed materials.

No texture was observed on the samples sputtered using Au as the seed material. The following textures were thus all obtained with Fe seed. At 500°C the (100) Si exhibited texture only in the region up to about 0.5 mm from the seed source. However, at 550°C, the (100) Si showed dense, uniform coning up to several mm from the seed source. The (111) Si developed cones at 550°C and again at 600°C. The cones were smaller and more densely packed on the (111) Si than they were in the (100) Si. Beyond about 2 mm from the shield edge, the Si (100) 600°C sample exhibited two distinct topographies, an extremely dense texture and a well developed cone texture (Fig. 5-5). This is the best texturing of Si on this scale that has been observed. The cone spacing averages about 1.1  $\mu$ .

ORIGINAL PAGE IS  
OF POOR QUALITY

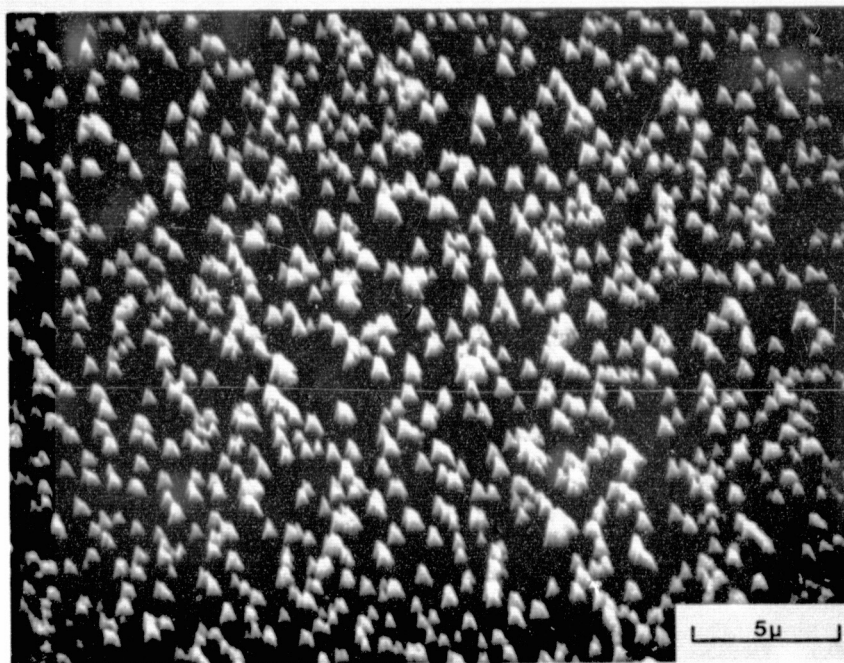


Fig. 5-5. Silicon seeded with Fe at 600°C.



## VI. CONCLUDING REMARKS

The texturing model based on surface diffusion and clustering of impurities has shown excellent agreement with experimental results both qualitatively and quantitatively. The existence of a minimum substrate temperature for texturing, the variation of cone distribution with substrate temperature and texturing with a high sputter yield seed on a lower sputter yield substrate were all predicted by this model. The model clearly has utility in facilitating the production of textured surfaces for a variety of applications such as low reflectance solar cells, heat collectors and radiators, and medical implants. The minimum critical temperature for cone formation is important in applications where a smooth sputtered surface is the desired end result. Because textured substrates are continuously cleaned by ion bombardment, the surface diffusion activation energies obtained should be those corresponding to a very clean surface.

The mathematical model for sputter seeding provides a means of predicting and controlling the seeding rate, an important parameter in texturing processes. Both seeding rate and uniformity are calculable for a variety of experimental sputtering configurations. In addition, knowledge of seeding density variation across a substrate provides a sensitive test of the concept of a critical temperature for seed clustering.

The rare gas interaction cross sections obtained will allow a more thorough analysis and understanding of a variety of energetic processes involved in ion beam and plasma devices. Cross sections in this energy range (1eV to 1KeV) have not previously been available.

These cross sections for elastic collision processes along with the previously calculated charge exchange cross sections allow designers of ion beam deposition and machining experiments to more readily arrive at appropriate configurations and pressure environments for beam propagation.

Experimental work on the operation of a broad beam ion source with  $\text{CF}_4$ , which readily breaks down into reactive species, allows limits to be placed on the operating lifetimes of the various source components in a very harsh plasma environment. There are significant problems with thermionic electron emitters as well as with significant material removed from such sensitive areas as the accelerator system.

## REFERENCES

### Section I

1. Robinson, R. S. and Haynes, C. M., "Surface Texturing", in NASA Contractor Report CR-135353, Nov. 1977.
2. Robinson, R. S., "Ion Beam Interactions", in NASA Contractor Report CR-135353, Nov. 1977.

### Section II

1. Berg, R. S. and Kominiak, G. J., "Surface Texture by Sputter Etching", J. Vac. Sci. Technol., Vol. 13, No. 1, Jan./Feb. 1977, pp. 403-405.
2. Robinson, R. S. and Haynes, C. M., "Surface Texturing", Industrial Ion Source Technology, NASA CR-135353, Nov. 1977, pp. 24-75.
3. Wehner, G. K. and Hajicek, D. J., "Cone Formation on Metal Targets during Sputtering", J. Appl. Phys., 42, Mar. 1971, pp. 1145-1149.
4. Cuomo, J. J., Ziegler, J. F., and Woodall, J. M., "A New Concept for Solar Energy Thermal Conversion", Appl. Phys. Lett., Vol. 26, No. 10, 14 May 1975, pp. 557-559.
5. Banks, B. A., Weigand, A. J., Babbush, C. A., and Van Kampen, C. L., "Potential Biomedical Applications of Ion Beam Technology", AIAA Paper No. 76-1018, AIAA International Electric Propulsion Conference, Key Biscayne, Florida, Nov. 14-17, 1976.
6. Hudson, W. R., "Nonpropulsive Applications of Ion Beams", AIAA Paper No. 76-1015, AIAA International Electric Propulsion Conference, Key Biscayne, Florida, Nov. 14-17, 1976.
7. Weigand, A. J. and Banks, B. A., "Ion-Beam-Sputter Modification of the Surface Morphology of Biological Implants", J. Vac. Sci. Technol., Vol. 14, No. 1, Jan./Feb. 1977, pp. 326-331.
8. Hudson, W. R., "Ion Beam Texturing", J. Vac. Sci. Technol., Vol. 14, No. 1, Jan./Feb. 1977, pp. 286-289.
9. Kittel, C., Introduction to Solid State Physics, Fifth Edition, John Wiley and Sons, Inc., 1976, p. 32.
10. Neumann, G. and Neumann, G. M., Surface Self-Diffusion of Metals, Diffusion Information Center, Bay Village, Ohio, 1972, pp. 49-60.
11. Butrymowicz, D. B., Manning, J. R., and Read, M. E., "Diffusion in Copper and Copper Alloys", J. of Phys. and Chem. Ref. Data, Vol. 2, 1973, pp. 643-655.

12. Neugebauer, C. A., "Condensation, Nucleation, and Growth of Thin Films", in Handbook of Thin Film Technology, 1970, pp. 8-3, 8-44.
13. Adamson, A. W., Physical Chemistry of Surfaces, 1976, pp. 372-384.
14. Somorjai, G. A., Principles of Surface Chemistry, Prentice Hall, Englewood Cliffs, New Jersey, 1972, p. 77.
15. Eisenhandler, C. B. and Siegel, B. M., J.A.P., Vol. 37, March 1966, p. 1613.

### Section III

1. Cooper, C. B. and Comas, J., "Angular Distribution of Sublimed and Sputtered Particles from Ag Single Crystals", J. App. Phys., Sept. 1965, 2891-2895.
2. Ramer, C. E., et. al., "Sputtering of Polycrystalline Copper and Silver by 30-170KeV Argon Ions", J. Appl. Phys., June 1964, 1673-1680.
3. Patterson, H. and Tomlin, D. H., "Experiments by Radioactive Tracer Methods on Sputtering by Rare Gas Ions", Proc. Roy. Soc., A 265, 1962, 474-488.
4. Wehner, G. K. and Rosenberg, D., "Angular Distribution of Sputtered Material", J. Appl. Phys., Jan. 1960, 177-179.
5. Gronlund, F. and Moore, W. J., "Sputtering of Silver by Light Ions with Energies from 2 to 12KeV", J. Chem. Phys., May 1960, 1540-1545.

### Section IV

1. Robinson, R. S., J. Vac. Sci. Technol., 15, 1978, 277-280.
2. Cuomo, J. J., Gambino, R. J., Harper, J. M. E., Kuptsis, J. D., and Webber, J. C., J. Vac. Sci. Technol., 15, 1978, 281-287.
3. Kaufman, H. R., J. Vac. Sci. Technol., 15, 1978, 272-276.
4. Harper, J. M. E., Cuomo, J. J., Gambino, R. J., Kaufman, H. R., and Robinson, R. S., J. Vac. Sci. Technol., 15, 1978, 1597-1600.
5. Spitzer, L., Jr., Physics of Fully Ionized Gases, Interscience, 1962, pp. 148-151.
6. Robinson, R. S., "Ion Beam Interactions", in NASA Contractor Report CR-135353, November 1977.
7. Goldstein, H., Classical Mechanics, Addison-Wesley, 1950, pp. 58-82.

8. Evans, R. D., The Atomic Nucleus, McGraw-Hill, 1955, pp. 828-851.
9. Barker, J. A., Fisher, R. A., and Watts, R. O., Molecular Phys., Vol. 21, 1971, 657-673.
10. Barker, J. A., Watts, R. O., Lee, J. K., Schafer, T. P., and Lee, Y. T., J. Chem. Phys., 61, 1974, 3081.
11. Bingham, F. W., J. Chem. Phys., 46, 1967, 2003-2004
12. Everhart, E., Carbone, R. J., and Stone, G., Phys. Rev., 98, 1955, 1045-1049.
13. Everhart, E., Stone, G., and Carbone, R. J., Phys. Rev., 99, 1955, 1287-1290.
14. Heer, C. V., Statistical Mechanics, Kinetic Theory, and Stochastic Processes, Academic Press, New York and London, 1972, p. 132.